

A universal perovskite nanocrystal ink for high-performance optoelectronic devices

Hochan Song^{1,†}, Jonghee Yang^{2,†}, Woo Hyeon Jeong^{1,†}, Jeongjae Lee^{3,†}, Tack Ho Lee⁴,
Jung Won Yoon¹, Hajin Lee⁵, Alexandra J. Ramadan⁶, Robert D. J. Oliver⁶,
Seong Chan Cho⁵, Seul Gi Lim¹, Ji Won Jang¹, Zhongkai Yu⁷, Jae Taek Oh¹, Eui Dae Jung⁸,
Myoung Hoon Song⁸, Sung Heum Park⁷, James R. Durrant⁴,
Henry. J. Snaith⁶, Sang Uck Lee⁵, Bo Ram Lee^{7,*} and Hyosung Choi^{1,*}

¹Department of Chemistry, Research Institute for Convergence of Basic Sciences, and Research Institute for Natural Science, Hanyang University, Seoul 04763, Republic of Korea

²Institute for Advanced Materials and Manufacturing, Department of Materials Science and Engineering, University of Tennessee, Knoxville, TN 37996, United States

³School of Earth and Environmental Sciences, Seoul National University Seoul 08826, Republic of Korea

⁴Department of Chemistry and Centre for Processable Electronics, Imperial College London, London W12 0BZ, United Kingdom

⁵Department of Applied Chemistry, Center for Bionano Intelligence Education and Research, Hanyang University, Ansan 15588, Republic of Korea

⁶Department of Physics, University of Oxford, Clarendon Laboratory, Parks Road, Oxford, OX1 3PU, United Kingdom

⁷Department of Physics, Pukyong National University, Busan 608-737, Republic of Korea

⁸Department of Materials Science and Engineering, Ulsan National Institute of Science and Technology (UNIST), Ulsan 44919, Republic of Korea

[†]These authors contributed equally: Hochan Song, Jonghee Yang, Woo Hyeon Jeong, Jeongjae Lee.

*e-mail: brlee@pknu.ac.kr; hschoi202@hanyang.ac.kr

Keywords: Perovskite nanocrystal, solution-phase ligand exchange, light-emitting diode, photovoltaics.

Abstract

Semiconducting lead halide perovskite nanocrystals (PNCs) are regarded as promising candidates for next-generation optoelectronic devices due to their solution processability and outstanding optoelectronic properties.^[1-13] While the field of light-emitting diodes (LEDs) and photovoltaics (PVs), two prime examples of optoelectronic devices, has recently seen a multitude of efforts towards high-performance devices based on PNCs, realizing both devices with high efficiencies and stabilities through a single PNC processing strategy has remained a challenge. Herein, we demonstrate that diphenylpropylammonium (DPAI) surface ligands, found through a judicious *ab initio* based ligand search, provide a solution to this problem. Our universal PNC ink with DPAI ligands, which is prepared through a solution-phase ligand exchange process, simultaneously allows single-step processed LED and PV devices with peak electroluminescence external quantum efficiency of 17.00 per cent and photovoltaic power conversion efficiency of 14.92 per cent, respectively. We reveal that a careful design of the aromatic rings such as in DPAI is the decisive factor in bestowing such high performances, ease of solution processing, and improved phase stability up to 120 days. Our work illustrates the power of ligand design in producing nanocrystal ink formulations for high throughput production of optoelectronic devices; it also paves a path for ‘dual-mode’ devices with both PV and LED functionalities.

Main

Inorganic lead halide-based perovskite nanocrystals (PNCs) have recently received great attention as next-generation semiconductors, attributed to their excellent and tunable optical properties, ease of solution processability, and improved thermodynamic stability in terms of phase transition.^[1-12] These advantages have led PNCs to be promising candidates for future optoelectronic applications, especially light-emitting diodes (LEDs) and photovoltaics (PVs).^[8, 10, 13] However, while LEDs and PVs share many similarities in terms of general device structure, their fundamental operating principles differ crucially: LEDs emit photons arising from radiative *recombination* of hole-electron pairs injected with a strong *external* bias, whereas PVs produce photocurrent from *separation* of photon-generated excitons by relatively weak *internal* electric fields. Subsequently, the requirement for favorable electrical coupling amongst the PNCs and electron/hole transport layer, whilst also important for efficient LED operations, becomes more stringent for PVs to ensure minimal loss of energy in forms of e.g., charge recombination.

On the other hand, practical realization of these optoelectronics starts from the synthesis of monodisperse and uniformly shaped PNCs, which necessitates the use of long organic chain ligands such as oleate (OA^-) and oleylammonium (OAm^+) to ensure well-dispersed NCs. Although required for synthesis, these ligands are typically poor in terms of charge conduction and moisture tolerances; hence, as-synthesized PNCs covered with long aliphatic ligands are not suitable for direct application to optoelectronic devices.^[8, 14-16] For PV applications where this problem of efficient charge transport is crucial for achieving high efficiencies, chemical treatments of the PNCs via layer-by-layer (LBL) process are generally employed to remove such insulating ligands and subsequently passivate the surface with short ligands and/or organic/inorganic halide salts.^[8, 9, 17-19] While this approach allows construction of electronically coupled PNC active layer for high photocurrents, the requirement for effective removal of ligands dictates that the overall LBL process should be repeated several times to attain active layers of sufficient thickness. The time-consuming nature of this procedure has been pointed as a major challenge in large-scale application of PNC-based PVs.

Meanwhile, for LED applications, it is common that the native ligands on the PNCs (OA^- , OAm^+) are replaced to functional ligands, which have stronger binding affinity to the surface as well as good interaction with solvents, resulting in well-dispersed PNC ink formulations more amenable to large-scale printing.^[13,15] The resulting PNC inks after solution-phase ligand

exchange (SPLE) exhibit minimal surface defects and high colloidal stability in solvents, which is suited for single-step fabrication of emissive films with conformal morphology. In light of this, one can expect that PNC-based PVs could also significantly benefit from a similar ink-based production strategy, if a ligand could be found to allow (1) a high degree of NC dispersion in solvents and (2) a good charge conduction through the NC interfaces.^[20-23]; no PNC PV devices prepared with ink-based single-step processing technique has been reported to date. This is an important aspect for commercialization of large-scale PV panels: deposition in ink forms enables delicate thickness control over the highly-passivated PNC film with a single-step process, thereby replacing the time- and effort-consuming LBL-based fabrication methods. Furthermore, more efficient passivation of the bare PNC surface is likely to inhibit the notorious phase transition of perovskite structures to photo-inactive phases (e.g. γ -CsPbI₃) and/or prevent moisture-induced degradation of perovskite structures, two phenomena which also plague PNC-based LEDs.^[2-5, 12, 24]

Herein, we present a solution to this combined scientific and engineering challenge of producing well-dispersed colloidal CsPbI₃ PNC inks demonstrating superior charge transport/injection and temporal stability under atmospheric conditions. Notably, this ink enables single-step processing of high-performance PV and LED devices. Through an *ab initio* based search, we identify that polarizability of the aromatic ligands, combined with their stronger binding affinities, enables both stable colloidal inks in weakly-polar solvent and simultaneously excludes the native ligands upon SPLE.^[25, 26] Among the various aromatic ligands, 3,3-diphenylpropylammonium iodide (DPAI) is expected to produce the highest concentration of PNC dispersion in toluene while retaining the conductivity over NC surface. Experimentally realized DPAI-PNC ink allows single-step fabrication of *both* LED and PV devices with remarkable optoelectronic characteristics – a peak external quantum efficiency (EQE_{peak}) of 17.0% for deep-red LED, and power conversion efficiency of 14.92% for PV. We further demonstrate that DPAI confers long-term phase and performance stability of photoactive α -CsPbI₃ PNC films over 4 months, attributed to enhanced blocking of moisture penetration by diphenyl rings. Our first demonstration of such PNC ink formulation for both LED and PV devices may be extended to other perovskite-based optoelectronics, therefore potentially making it a ‘universal’ PNC ink; we also show that its application may further extend to produce efficient ‘dual-mode’ devices with both PV and LED functionalities.

Choice of diphenylpropylammonium ligand through an *ab initio* based search. As described above, the organic ligand of choice suitable for developing PNC inks capable of producing high-performance photoactive layers in both LED and PV devices should meet the following major criteria: (1) good dispersion in solvents for producing highly concentrated ink, which can be achieved by ligands with large dipole moments; (2) small barrier for charge conduction across the ligand, which in general requires unsaturated hydrocarbons with high-lying HOMO and/or low-lying LUMO levels; and (3) non-labile passivation of PNC surface defects, which necessitates ligands with strong binding to PNC surfaces. In addition, (4) the ligand should minimize moisture penetration, which is a significant factor for enabling stable long-term operation of PNC devices; finally, for a minor point, (5) the ligand should ideally be commercially available for mass production, although we do note that additional tailored improvements to the ligands with extra synthetic steps are indeed possible and may be required to further improve the device stability and performance.

While various organic functional groups can, and indeed have been shown to, satisfy one or more of these requirements, the second criterion essentially necessitates the use of unsaturated hydrocarbons, a strategy which has been widely used in organic conducting polymers. Thus, we choose phenyl group as the base component for our ligand, as it can easily meet the aforementioned criteria due to its chemical similarity to toluene, a widely used solvent for PNC inks, as well as its electron-rich polar aromatic ring which is likely to provide strong van der Waals interaction to perovskite surface and resistance to moisture. Thus, a series of phenylalkylammonium molecules were screened computationally with Density Functional Theory (DFT) methods by their surface binding energies to CsPbI₃ and solvation energies in various organic solvents (the surface model of CsPbI₃, binding energy calculation, and solvation simulation method are described in **Supplementary Note 1, 2 and Supplementary Fig. 1**). The results, which are shown in **Supplementary Fig. 2 and 3**, clearly demonstrates the strong binding of 3,3-diphenylpropylammonium (DPAm⁺) ligands to the CsPbI₃ perovskite surface (with the largest binding energy of -1.73 eV), with a significant portion of binding energy originating from the van der Waals interaction; furthermore, DPAm also shows more or less similar solvation energies in toluene with the rest of aromatic ligands (approximately -1.42 eV). Also of note, DPAm⁺ is expected to bind more strongly to the PNC surface than OAm⁺, the prototypical ligand used in PNCs which also suffers from chemical liability or ‘dynamic binding’; this phenomenon is known to result in substantial atomic voids, such as cesium and iodine vacancies (i.e., V_{Cs} and V_I, respectively) as surface defects (**Fig. 1a**).^{[8, 9, 17,}

^{21, 27-29]} Thus, treatment of as-synthesized PNCs with the iodide salt of DPAm⁺ (DPAI) and subsequent washing with *n*-hexane is expected to yield PNC crystals with OAm⁺ ligands substituted by DPAm⁺ ligands (sharing the same ammonium functional group) by virtue of differences in their binding energies and solubility in *n*-hexane. This modified SPLE process is schematically illustrated in **Fig. 1b**.

Ligand-exchanged DPAI-PNC ink shows high colloidal stability and enhanced optical properties. Based on this prediction, as-synthesized CsPbI₃ PNC sample decorated with OA⁻ and OAm⁺ ligands was subject to SPLE processes with various phenylalkylammonium iodide salts. The result of this screening, as shown in **Supplementary Fig. 4**, clearly shows that DPAI is the only salt which can produce stable colloidal dispersion of PNCs capable of passing through a syringe filter. All other ligands, apart from phenylammonium (PAm⁺), resulted in severe agglomeration and/or fusion of NCs; note that while treatment with PAm⁺ iodide seems to generate a stable dispersion, PAm⁺ does not actually participate in a ligand exchange with OAm⁺ species, therefore resulting in the same native PNC stock. This non-exchanging behavior is in accordance to previous reports and confirmed here using solution-state nuclear magnetic resonance (NMR) experiments (*vide infra*)^[3, 30]. Transmission electron microscopy (TEM) analysis also revealed that only the SPLE-PNC prepared with DPAI retained the original size and shape (**Fig. 1c, d** and **Supplementary Fig. 5**), whereas the use of other ligands resulted in severe amalgamation of PNCs, destroying the colloidal dispersion (**Supplementary Fig. 6**). This implies that the diphenyl rings in DPAm⁺ play a decisive role during SPLE, preventing the PNC surface from the deleterious effects observed from mono-phenyl counterparts while retaining the colloidal characteristics of PNCs; in particular, these phenyl rings are crucial for providing selective dispersion in weakly polar solvents (toluene, chlorobenzene, and chloroform). In contrast, neat (as-synthesized) PNCs with OAm⁺ and OA⁻ could be dispersed in both these weakly polar solvents and nonpolar *n*-hexane (**Fig. 1e and 1f**). Thus, a high concentration SPLE-PNC ink (>150 mg mL⁻¹) with surface DPAm⁺ ligand was realized by exploiting this difference in ligand solubilities.^[26]

Experimental evidences for ligand exchange with DPAm⁺ were sought with solid-state ¹³C NMR, corroborated by solution-state ¹H NMR and Fourier-transform infrared (FTIR) spectroscopies. Due to the pronounced ¹³C chemical shift of *ipso*-phenyl carbon away from the (overlapping) resonances of other ligands, ¹³C solid-state NMR of PNCs offers the most direct

proof for the proposed ligand exchange. The ^{13}C solid-state NMR spectra of solid DPAl, together with those of neat and SPLE-PNCs, are shown in **Fig. 1g**. The presence of *ipso*-phenyl carbon peak (143.7 ppm; green dot) in the SPLE-PNC sample clearly exhibits the presence of DPAm⁺ ligands on the surface of PNCs after the ligand exchange. Nevertheless, the ^{13}C spectra also reveal the presence of residual OAm⁺ ligands after the SPLE process, manifested by a shoulder peak at 42.0 ppm (olive dot, **Fig. 1g**) to the DPAm⁺ signal (orange dot); this indicates that the ligand exchange process is only partially complete, which may arise from a competitive binding action between OAm⁺ and DPAm⁺ sharing the same ammonium binding motif. While a full ligand exchange would be desirable in terms of charge carrier mobility, the clear presence of DPAm⁺ molecules with unsaturated phenyl groups is likely to contribute to the enhanced conductivity. Concurrent with this substitution, a near-complete removal of OA⁻ is observed; the resulting surface void sites are most likely passivated by additional iodide anions from DPAl,^[30] as evidenced from X-ray photoelectron spectroscopy of resulting films (*vide infra*).

On the other hand, solution-state ^1H NMR spectroscopy of dissolved PNC solution provides quantification of ligands on the PNC surface (**Supplementary Fig. 7**). Through integration of alkene and phenyl peak intensities (5.3 and >7.0 ppm, respectively) with respect to an internal ferrocene standard,^[21, 29, 30] ligand densities on the PNC surface before and after SPLE were estimated. The result revealed that the extent of ligand substitution is roughly proportional to binding affinity of the aromatic ligands, with DPAm being the densest with 0.91 molecules/nm² PNC surface while PAm⁺ shows significantly low density with only 0.23 molecules/nm², in line with the computational predictions on binding affinities and prior experimental reports.^[30] These NMR results are also supported by FTIR measurements of PNC dispersion (**Supplementary Fig. 8**): the aromatic stretching/bending modes at $\sim 1490\text{ cm}^{-1}$ and $< 1200\text{ cm}^{-1}$ appeared gradually growing in intensity with increase in the surface binding energy of the ligands.^[3, 17, 31-33]

As evidenced in prior studies, these collective passivating actions of DPAm⁺ and I⁻ ions are likely to enhance the radiative properties of PNC without altering its emission wavelength.^[34, 35] In line with this prediction, the SPLE-PNC using DPAl retained the original optical bandgap (681 nm) while exhibiting improved solution photoluminescence quantum yield (PLQY) from 72% to 90% and longer exciton lifetime (**Supplementary Fig. 9a and b**, respectively).^[3, 9, 27, 28, 36] These observations suggest that the DPAl treatment effectively passivates the defects on PNC surface without compromising its dimensionality;^[27, 28] the resulting enhancement in

solution-state optoelectronic characteristics is likely to be carried over to the deposited films, which we now discuss.

Defect suppression and superior conductivity of DPAI-based SPLE-PNC films. For application in optoelectronic devices, the PNCs must be cast into films via solution processing. To attain high device performances, the PNCs thus should not only show excellent optoelectronic properties in colloidal form, but also exhibit favorable mesoscopic characteristics such as facile charge carrier conduction and homogeneous surface morphology in the final film. As outlined in the introduction, the traditional method of processing electrically coupled thick PNC films was performed with time-consuming multistep LBL approach, where the long-chain ligands are repeatedly stripped off after application of PNC solution. In contrast, here we demonstrate the capability of concentrated DPAI-passivated SPLE-PNC ink to generate films of better quality through single-step deposition.

PL spectra of neat, LBL-, and SPLE-PNC films are shown on **Fig. 2a**. Crucially, the SPLE-PNC film exhibited the strongest PL intensity (2-fold and 10-fold enhancements from neat and LBL-PNC films, respectively) with the highest PLQY of 85% (**Supplementary Fig. 10**). This suggests that defect passivation of the SPLE-PNC with DPAm^+ and I^- ions was not compromised during film deposition with a concentrated ink, as further confirmed from the longest exciton lifetime in this film observed through time-resolved PL data. (**Supplementary Fig. 11**). To further ascertain the defect passivation, X-ray photoelectron spectroscopy (XPS) was performed on the PNC films (**Supplementary Fig. 12**). For all elements, marginal peak shifts toward lower binding energy were commonly observed from SPLE-PNC film, as a signature of improved stoichiometry by additional iodide passivation.^[37] Indeed, the estimated I to Cs ratio of the DPAI-PNC film exhibited more balanced stoichiometry (value closer to 3), strongly supporting this hypothesis (**Fig. 2b**).^[38] The slight increase of the ratio in LBL-PNC would be attributed to the strip-away of Cs^+ by repetitive washing during LBL process, conversely highlighting the disadvantage of the classical method.

Femtosecond-transient absorption (fs-TA) spectroscopy further reveals the influence of defect passivation on the exciton dynamics of the PNC films. **Fig. 2c** shows fs-TA spectrotemporal maps of the PNC films, showing the ground-state bleach (GSB) signals at the corresponding band-edge positions (~ 680 nm).^[4, 18] Clearly, SPLE-PNC exhibited the longest-lived GSB decay kinetics where the largest portion of excitons survived at time delays up to 6

ns (**Supplementary Fig. 13**). From the decay dynamics of these GSB signals (all exhibiting mono-exponential decays), corresponding lifetimes of excitons were estimated to be 3.52, 1.14, and 7.87 ns for neat, LBL-, and SPLE-PNC, respectively (**Supplementary Fig. 14**). These results are in parallel with the magnitude of defect passivation on the PNC surface, as observed from the XPS analysis. The stripping action of surface Cs^+ and I^- in the LBL process is expected to be directly responsible for exciton dissipation through creation of surface defect sites, resulting in shorter exciton lifetimes. In contrast, preserved defect passivation by the SPLE process with DPAI effectively reduces the number of such trap sites, allowing excitons to survive with much longer lifetimes. Note that the acceleration of exciton decay, by increasing the pump fluence, is pronounced the most in LBL-PNC, compared with the other PNC films (**Supplementary Fig. 15**). This further corroborates that the excitons are mainly dissipated by surface defects, rather than the ligands coordinating the PNC surface.

The SPLE-PNC film also shows the largest red-shift of band edge, a phenomenon which is suggestive of enhanced electronic coupling between the PNCs (**Supplementary Fig. 16**).^[2, 3] As this electrical coupling is expected to be crucial for optoelectronic devices and especially PVs, charge transport behavior in PNC matrices was measured with charge-selective photo-induced charge extraction by linearly increasing voltage (photo-CELIV) experiments. Using this technique, photocurrent transients solely associated with either electrons or holes, produced after exciton dissociation, could be collected (**Supplementary Fig. 17a and b**).^[39-41] In-depth assessments of these signals provide quantitative insights regarding the charge transport through mobility and recombination dynamics for each type of photocarriers flowing through the PNCs, as exhibited in **Supplementary Fig 17c and d** (see **Methods** for the details on the models used for quantitative estimation).^[39, 40] First, we consider the carrier mobility which was estimated from the time-dependent photocurrent response of the PNC films. The result, which is shown in **Fig. 2d**, unambiguously demonstrates that the carrier mobility increased significantly in SPLE-PNC films, the effect being more pronounced for holes: almost threefold enhancement was observed for the SPLE-PNC films relative to its LBL-PNC counterpart (hole mobilities of 0.96 and $2.92 \times 10^{-3} \text{ cm}^2 \text{ V}^{-1} \text{ s}^{-1}$ for LBL- and SPLE-PNC films, respectively). Similar increase in electron mobilities was also observed, although the magnitude is somewhat modest (a two-fold increase from 0.57 and $1.02 \times 10^{-3} \text{ cm}^2 \text{ V}^{-1} \text{ s}^{-1}$). At the same time, charge recombination is effectively suppressed in the SPLE-PNC films (mirrored as increased recombination time constant).

Since both the carrier mobility and charge recombination depends critically on the presence of PNC surface defects,^[42, 43] these may be attributed to improved surface passivation of SPLE-PNC by a combined action of DPAm⁺ and I⁻ ions. This conclusion is also in line with the observations from the above section: the surface passivation by the ligand reduces the amounts of V_{Cs} and V_I, generally serving as energetically shallow traps that retarding carrier transport (via trapping-detrapping process).^[42, 43] Note that, however, the extents of mobility suppression known to be responsible for the shallow traps are relatively smaller (decreased by ~10%),^[42] this suggests that alternative mechanisms are likely to be responsible for the observed two- and three-fold enhancements in carrier mobilities (for electrons and holes, respectively) of the SPLE-PNC matrix. While further experimental and computation investigation is in progress with respect to the exact role of DPAm⁺ ligand, we postulate that the presence of electron-rich aromatic ring is crucial for such phenomena: attractive dispersion interaction between the ligands on individual PNCs may allow a denser, uniform packing of nanocrystals electronically coupled through the π -conjugated aromatic rings of DPAm⁺.^[31, 32] In contrast, nominally bare PNCs after the LBL process is likely to experience some degree of electrostatic repulsion between the same type of charged perovskite surfaces covered with Cs⁺, which may contribute to a sloppier packing and poor degree of inter-NC carrier mobility. This is evidenced from the AFM surface profiles (**Supplementary Fig. 18**) of each PNC films: the surface of SPLE-PNC prepared with a concentrated ink demonstrated a homogeneous, flat surface with a root-mean-square roughness (R_q) value of 3.58 nm compared to those of neat and LBL-PNC film (10.63 and 11.63 nm, respectively), also confirmed from scanning electron microscopy (SEM) images (**Supplementary Fig. 19**). Note that the neat PNC cannot provide conformal film as demonstrated by SPLE-PNC ink even when the same concentration and solvent were employed (**Supplementary Fig. 20**). Thus, formation of uniform films through use of SPLE-PNC ink is beneficial for not only inter-layer charge transport but for the intra-perovskite layer mobility as well, the added degree of electronic coupling over the PNC matrix being manifested as notable enhancements in carrier mobilities.

Finally, estimates on carrier diffusion lengths can also be obtained from the photo-CELIV measured values of carrier mobility and lifetime (i.e., recombination time constant; **Fig. 2e**).^[39, 44] Both the electron and hole diffusion lengths, qualitatively consistent with the values from previous reports,^[4, 9, 38] were noticeably enhanced (for both electrons and holes) in SPLE-PNC matrix; the degree of enhancement was larger for holes (~two-fold from 174 to 383 nm) when compared to that of electrons (~1.6-fold from 115 to 185 nm), which may be attributed to the

much better hole mobility as discussed above.

Together, these observations suggest that the SPLE-PNC ink with DPAI ligand exchange allows single-step processed PNC films with superior defect suppression with flat film surfaces and improved electrical coupling between the PNC particles, thereby resulting in a significant improvement of optoelectronic performances.

Single-step processed SPLE-PNC films allow efficient LED and PV devices with excellent temporal stability and dual-mode operation. To assess the performance of our ink-deposited SPLE-PNC films against the neat and traditional LBL-PNC films for optoelectronic applications, both LED and PV with classical device architectures were fabricated (**Fig. 3a and 3b**). Here, the neat and LBL-PNCs respectively served as an emissive layer and active layer in LED and PV (as control devices), and the SPLE-PNC was employed to both types of layers in each device (as target devices). The surface chemistry and packing behaviors of PNC films after each preparation method are also schematically illustrated in **Fig 3c**. Marginal difference in energy levels were observed for all three samples (**Supplementary Fig. 21**), which is expected to pose only minor effects in terms of energy level matching for the charge injection and transport processes in LED and PV, respectively. Cross-sectional SEM images of the LED and PV devices employing SPLE-PNC are also shown in **Supplementary Fig. 22**. These images confirm the rigidity of the PNC layer constructed via *single*-step deposition (up to ~450 nm), the structure of which is maintained upon deposition of the above layer.

As expected from the optical responses of PNC colloids and standalone films, significant improvements were observed for the current density-voltage-luminance (*J-V-L*) and EQE curves (as a function of injection current) of the champion LEDs (**Fig. 3d and 3e**, respectively). The target device reproducibly demonstrates 18-fold and 15-fold enhancements in maximum luminance (L_{\max} , 657 cd/m²) and EQE_{peak} (17.00%) compared to the control devices (**Table 1 and Supplementary Fig. 23**). The target device also exhibited lower turn-on voltage (V_{TO} , the voltage when the luminance exceeds 0.1 cd/m²) of 2.8 V. Also the target device demonstrated consistent deep-red EL emission (peak centered at 684 nm) as increasing external voltage, confirming that the emission zone exclusively confined within the PNC (**Fig. 3f**). Such excellent deep-red LED performances by employing SPLE-PNC (**Supplementary Table 1**) would be attributed to complete defect passivation and augmented electronic coupling over the PNC matrix, as extensively characterized above. These would maximize the actual emissive

zone in the PNC layer, with higher probability for radiative recombination (~85%). Additionally, the target LED demonstrated a decent operation stability over 80 min, without involving noticeable EL shifts (**Supplementary Fig. 24**).

Fig. 3g exhibits J - V curves of the champion PVs, and the EQE spectra of corresponding devices are also displayed in **Fig. 3h**. The PCE of target PV (14.92%) outperformed that of control (13.22%) with a reliable reproducibility (**Supplementary Fig. 25**). Even though the SPLE-PNC active layer was prepared via a single-step deposition with a concentrated ink, at the optimized PNC thickness, concurrent enhancements in open-circuit voltage (V_{OC} , 1.21 V), short-circuit current density (J_{SC} , 16.64 mA/cm²), and fill factor (FF, 73.89%) were achieved (**Table 1** and **Supplementary Fig. 26**). Transient photovoltage and photocurrent measurements revealed that, the target PV exhibited longer carrier lifetime (63.13 μ s) as well as faster carrier transit time (2.14 μ s) (**Supplementary Fig. 27**). Combining with evidences from fs-TA, this suggests that SPLE-PNC minimizes photocarrier dissipation by suppressing the band-tail trap states, thereby resulting in concurrent enhancements.^[45-47] It should be noted that, to the best of our knowledge, this is the first demonstration of PV employing single-step deposited PNC active layer, and achieving comparable PCE with LBL-PNC based PVs (**Supplementary Table 2**).^[19, 38]

Strikingly, we observed that, under ambient condition (relative humidity of 25~35%), SPLE-PNC exclusively exhibited a decent phase stability, retaining the photoactive black phase over 4 months (**Fig. 4a and b**); the target PV also retained its initial PCE over 40 days and exhibited 73% retention after 103 days under ambient air without encapsulation (**Fig. 4c**), the best PNC-based PV stability reported so far.^[2, 3, 17] This enhancement may also be attributed to the action of aromatic DPAm⁺ ligand: as DPAm⁺ is overall less flexible than long-chain OAm⁺/OA⁻ ligands, substitution of the latter after DPAI treatment is also expected to result in denser packing of molecules and reduced degree of moisture penetration through the surface ligands, which is known to cause the phase transition to non-photoactive orthorhombic γ -CsPbI₃.^[2, 3, 17] This speculation is confirmed with molecular dynamics (MD) simulations (The multi-ligand occupied models and dynamics methods are described in **Supplementary Note 3**), which conclusively demonstrate that the diphenyl rings of DPAm⁺ are very effective in blocking moisture penetration into the PNC lattice, while OAm⁺ shows presence of significant water concentration in the region occupied by surface ligands (**Fig. 4d-g**, **Supplementary Fig. 28** and **Supplementary Video 1**); this enhanced encapsulating effect confers outstanding phase

and performance stability for the SPLE-PNC devices.

Finally, exploiting the superior electrical coupling and defect passivation in single-step ink deposited films, a dual-mode hybrid device capable of both PV and LED functionalities was fabricated from SPLE-PNC ink. The operation of this device in both modes is shown in **Supplementary Video 2**. While significant improvements in terms of device configuration and performances are required for a full-scale adaptation of this device, future applications of such dual-mode devices may include outdoor billboards which can independently generate and store energy as PVs during daylight and display video advertisements as LED screens when dark. In this regard, the dual-mode functionality enabled by SPLE-PNC may pave a path toward developments of standalone ‘ubiquitous display’ devices.

Outlook

In conclusion, for the first time, a universal PNC ink directly applicable to both LED and PV via modified SPLE process with DPAI aromatic-iodide pair was developed. This yielded well passivated and highly concentrated PNC ink without sacrificing its optical characteristics and dimensionality. Through a judicious *ab initio* screening of possible ligands, we identify that DPAm⁺, associated with the diphenyl ring structure compared to classical mono-phenyl ring, confers several outstanding characteristics which leads to electronically-coupled, homogeneous and device-grade-thick SPLE-PNC film with little surface defects in a single-step deposition. Remarkably, the same SPLE-PNC ink can be used to fabricate LED as well as PV devices, both with outstanding performances (efficient deep-red LED with EQE_{peak} of 17.00% and PV exhibiting PCE of 14.92%) without the time-consuming LBL process. This ‘universal’ PNC ink is also capable of producing a single device which can function as both PV and LED. The multifaceted nature of DPAm⁺ ligand also allows SPLE-PNC film with excellent ambient stability over 4 months and the resulting PV with 73% retention after 103 days without encapsulation. Our rational design strategy provides a key example for selecting ligands with multiple functions for passivating and stabilizing PNCs, therefore providing a new avenue for mass production of high-performance optoelectronics via a universal PNC ink.

Acknowledgments

This research was supported by Nano-Material Technology Development Program through the

National Research Foundation of Korea(NRF) funded by Ministry of Science and ICT (NRF-2021M3H4A1A02049634, NRF-2019R1A6A1A10073437, and NRF-2021R1A2B5B01002879). NMR data were acquired on a 400-MHz solid-state NMR spectrometer (AVANCE III HD, Bruker) at KBSI Western Seoul Center. We thank Dokyung Kim and Dr. Seen Ae Chae for helping with NMR measurements.

Methods

Materials

Cesium carbonate (99.9%), lead iodide (PbI_2 ; 99.999%), 1-octadecene (ODE, 90% tech.), oleylamine (OLA, 70% technical grade), oleic acid (OA, 90% tech.), methyl acetate (MeOAc, anhydrous 99.5%), toluene (anhydrous 99.8%), n-hexane (anhydrous, 95%), chlorobenzene (anhydrous 99.8%), octane (anhydrous, $\geq 99\%$), chloroform (anhydrous $\geq 99\%$), hydrochloric acid (HCl, ACS reagent, 37%), lead nitrate ($\text{Pb}(\text{NO}_3)_2$, 99.999% trace metals basis), titanium ethoxide ($\geq 97\%$), bis(trifluoromethane)sulfonamide lithium salt (Li-TFSI), 4-tert-butylpyridine (4-tBP; 96%), acetonitrile (anhydrous, 99.8%), 3,3-diphenylpropylamine (DPA, 97%), 3-phenyl-1-propylamine (PPA, 98%), hydriodic acid (HI; 57 wt.% in H_2O), diethyl ether (anhydrous, ACS reagent $\geq 99.0\%$), 1-butanol (anhydrous, 99.8%) and poly[(9,9-dioctylfluorenyl-2,7-diyl)-co-(4,4'-(N-(4-sec-butylphenyl)diphenylamine))] (TFB) were purchased from Sigma-Aldrich. Phenylammonium iodide (PAI) and benzylammonium iodide (BAI) were purchased from Greatcell Solar. Ethanol (99+%) and MoO_3 (99.9995%) were purchased from Alfa Aesar. 2,2',7,7'-tetrakis(N,N-di-p-methoxyphenylamine)-9,9'-spirobifluorene (Spiro-OMeTAD; $\geq 99.5\%$) was purchased from Lumtec. Indium-tin oxide (ITO; $\sim 4.5\Omega/\text{sq}$) and fluorine-doped tin oxide (FTO; $7\Omega/\text{sq}$) transparent conductive substrates were purchased from AMG. Aqueous solution of PEDOT:PSS (Clevios AI 4083) was purchased from Heraeus. Poly[bis(4-phenyl) (4-butylphenyl) amine] (poly-TPD) and 2,2',2''-(1,3,5-benzinetriyl)tris(1-phenyl-1-H-benzimidazole) (TPBi; 99.9%) were purchased from OSM. LiF (99.9%), Al (99.999%) and Ag (99.99%) were purchased from iTASCO.

Synthesis of ligand salts

DPAI was synthesized by reacting DPA with HI. DPA solution in absolute ethanol was cooled to 0°C in an ice bath and slightly excessive HI was slowly added into the solution. The reaction mixture was stirred for overnight under inert gas condition. Same protocol was used to synthesize PPAI by reacting PPA with HI. After stirring, the solutions were evaporated using a rotary evaporator to yield ligand salts. These products were washed with diethyl ether more than three times and dried at 60°C for 12 h in an oven. The other ligand salts (i.e., PAI and BAI) were used for experiments as-purchased.

Synthesis of CsPbI₃ PNCs and SPLE protocols

A similar synthetic protocol for the CsPbI₃ PNCs from the previous literature was utilized with a slight modification.^[6]

Cesium-oleate solution: Cs₂CO₃ (0.407g), 1.25 mL of pre-degassed OA and 20 mL ODE were put into a 100 mL 3-neck flask and degassed under vacuum at 120 °C for 1h. After degassing, N₂ gas was filled into the flask and then the solution was elevated to 140 °C, which is ready for injection.

CsPbI₃ PNCs synthesis: PbI₂ (0.5g), 2.5 mL pre-degassed OA, 2.5 mL pre-degassed OLA and 25ml ODE were put into 100 mL 3-neck flask and degassed under vacuum at 120 °C for 1h. After degassing, N₂ gas was filled into flask and then the temperature was increased to 180 °C. When the temperature reaches 180 °C, Cesium-oleate solution (2 mL) was swiftly injected into flask. After 10 s, heating mantle was removed and the flask was cooled with an ice bath.

Purification: 15 mL of crude PNC dispersion and 35 mL of MeOAc (as an anti-solvent) were mixed and centrifuged at 8,000 rpm for 5 min. After that, the supernatant was discarded and the remaining PNCs were re-dispersed in 5 mL of hexane. After then, 8 mL of MeOAc was added to the PNC dispersion and centrifuged at 8,000 rpm for 5 min. The purified PNCs, after discarding the supernatant, were re-dispersed in 5 mL of n-hexane, filtered with a 0.2 μm PTFE syringe filter (Whatman), and stored prior to use.

SPLE protocol: purified CsPbI₃ PNCs are dispersed in toluene (30 mg mL⁻¹). 120 μL of DPAI solution (83.3 mg mL⁻¹ in toluene:1-BuOH 1:1 v/v) were added into NCs dispersion and stirred for 3 min. For the SPLE with the other ligand salts, equimolar solutions were prepared (as same with DPAI solution). The solutions were added into the PNC stock dispersion and stirred for 3 min. For purification, 5 mL MeOAc was added to 1 mL of the exchanged PNC dispersion 1 mL, and centrifuged at 10,000 rpm for 5 min.

The final PNCs were dispersed in toluene (35 mg mL⁻¹) for LED fabrication and dispersed in chloroform (150 mg mL⁻¹) for solar cell fabrication.

Fabrication of PNC optoelectronics

LED fabrication: ITO substrates were washed by ultrasonic treatment in deionized water (DI water), acetone, and 2-propanol for 10 min each. After drying in an oven, the ITO substrates

were treated with O₂ plasma for 10 min. The PEDOT:PSS solution was spin-coated on ITO at 4,500 rpm for 40 s and annealed at 140 °C on the hotplate for 10 min. The substrates were transferred into a glove box. Poly-TPD (12 mg mL⁻¹ in chlorobenzene) layer was spin-coated on the PEDOT:PSS layer at 4,000 rpm for 40 s and annealed at 120 °C for 5 min. TFB (16 mg mL⁻¹ in xylene) layer was spin-coated on poly-TPD layer at 4,000 rpm for 40 s and annealed at 150 °C for 30 min. After deposited HTLs, PNC (35 mg mL⁻¹ in toluene) emissive layer was spin-coated on HTL layer at 2,000 rpm for 20 s. Finally, TPBi (75 nm), LiF (1 nm), and Al (100 nm) were sequentially deposited at ~10⁻⁶ Torr by using a thermal evaporator. A patterned shadow mask was employed to deposit Al electrodes with a fixed area. An active area of the LED (0.135 cm²) was defined by the cross-section between the patterned Al and ITO electrodes.

PV fabrication: FTO substrates were washed by ultrasonic treatment in deionized water (DI water), acetone, and 2-propanol for 10 min each. After drying in an oven, the FTO substrates were treated with O₂ plasma for 15 min.

TiO₂ solution (Titanium ethoxide 375 μL, EtOH 5 mL, DI water 125 μL, HCl 10 μL) was spin-coated on FTO substrate 3,000 rpm for 20 s and annealed at 150 °C and 500 °C for 60 min each. After deposition of TiO₂ ETL, SPLE-PNC (150 mg mL⁻¹ in chloroform) photoactive layer was spin-coated on the ETL at 800 rpm for 5 ss and 3,000 rpm for 20 s. For LBL-PNC PV, neat CsPbI₃ PNC dispersion (75 mg mL⁻¹ in octane) was spin-coated on ETL at 1,000 rpm for 10 s and 2,000 rpm for 10 s. And then, the PNC film was soaked with Pb(NO₃)₂ solution (1 mg mL⁻¹ in MeOAc) for 3 s and spin-dried, followed by washing with neat MeOAc. This procedure was repeated 4 times to get thick NC film (~300 nm). Spiro-OMeTAD solution (72.3 mg Spiro-OMeTAD, 28.8 μL 4-tBP, 17.5 μL Li-TFSI stock solution (520 mg mL⁻¹ in ACN), 1 mL in chlorobenzene) was spin-coated on perovskite layer 4,000 rpm for 30 s. Finally, patterned MoO₃ (12 nm) and Ag (120 nm) electrodes were sequentially deposited onto the samples at ~10⁻⁶ Torr by using a thermal evaporator. An active area of 0.055 cm² was defined by the fixed pattern of the electrodes.

Materials and device characterizations

XPS and UPS measurements were conducted using a photoelectron spectrometer (Thermo Fisher Scientific, Theta Probe) installed at the Hanyang LINC+ Analytical Equipment Center (Seoul). For XPS and UPS measurements, Al Kα (1486.7 eV) and He I (21.22 eV) beamlines were respectively used. For both measurements, a fixed sample-to-detector angle of 30° was

used to mainly collect surface-oriented signals. Solid-state NMR measurements were performed at 9.4 T (KBSI Western Seoul Center) using a 4 mm Bruker HXY probe. All samples were spun at 13 kHz MAS in zirconia rotors. Perovskite samples were packed under a nitrogen atmosphere. ^{13}C spectra were acquired using ^1H - ^{13}C Hartmann-Hahn cross polarization sequence with 100 kHz SPINAL64 ^1H decoupling. ^{13}C shifts are referenced to tetramethylsilane. ^1H NMR spectra were recorded with a 400 MHz NMR spectrometer (Bruker Avance III HD). FTIR spectra were recorded using PerkinElmer Spectrum Two FT-IR Spectrometer. XRD patterns were collected using a Rigaku SmartLab diffractometer.

SEM images were taken with Verios G4 UC (FEI) SEM instrument equipped at the Hanyang LINC + Analytical Equipment Center (Seoul). TEM images were taken using a JEM-2100F TEM instrument (JEOL). AFM images were obtained using an AFM instrument (Park Systems XE-100) operating in non-contact mode.

UV-Vis absorption spectra were measured with a Shimadzu UV-2600 UV-Vis spectrometer. Steady-state PL measurements were carried out using a pulsed xenon lamp. TRPL decays were collected with a time-correlated single-photon counting setup (FluoTime 300). A pulsed diode laser (He-Cd laser) operating at a wavelength of 520 nm was used as an excitation source. Each decay dynamics was fitted with exponential decay models and associated dynamic parameters were estimated by using a fitting software (FlouFit).

TPV and TPC measurements were conducted using a home-built setup consisting of a pulsed Nd:YAG laser (OPOTEK, VIBRANT 355 LD) with a repetition rate of 10 Hz and a pulse width of 5 ns, an oscilloscope (Agilent DSO3202A), and extra light output from a Xe lamp. The V_{OC} established by the continuous light was monitored using a Keithley 2400 sourcemeter.^[40,47] A small perturbation using a laser pulse ($\lambda=532$ nm) was applied to the samples, where the fluence was modulated using a series of neutral-density filters. A 1 M Ω input terminal and 50 Ω terminal resistor were respectively mounted to the oscilloscope for TPV and TPC measurements. For PeLEDs, J - V - L characteristics and device performances were measured using a Konica Minolta spectroradiometer (CS-2000) with a Keithley 2400 sourcemeter. PeLED device characteristics were measured under ambient air conditions. The J - V curves of PVs were measured using an LCS-100 Series Small Area Solar Simulator, mounted in a N_2 -filled glove box, with a Keithley 2400 sourcemeter. A simulated solar light with an Air Mass 1.5 Global (AM 1.5 G) with an irradiation intensity of 100 mW cm^{-2} was used. A black shadow mask with an aperture area of 0.031 cm^2 was employed to prevent

overestimation of photocurrent. The PV devices were just introduced into the glove box for the measurement and rapidly taken out (as unencapsulated) and stored under ambient air. External quantum efficiency spectra were collected using the PV measurement QE system by applying monochromatic light from a xenon lamp.

Transient absorption measurements

A Helios spectrometer (Spectra Physics, Newport Corp.) was used to measure the broadband pump-probe fs-TA spectra and kinetics for thin film samples. Ultrafast laser pulses (800 nm, 100 fs duration) were generated by a 1 kHz Ti:sapphire regenerative amplifier (Solstice, Spectra Physics, Newport Corp.). One portion of the 800 nm pulse was directed to an optical parametric amplifier (TOPAS Prime, Spectra-Physics) and a frequency mixer (Niruviz, Light Conversion) to tune the visible pump pulses at various wavelengths. The pump pulses were modulated at a frequency of 500 Hz by a mechanical chopper. The rest of the 800 nm pulse was routed onto a mechanical delay stage with a 6 ns time window and directed through a non-linear sapphire crystal to generate a white light probe ranging for the visible region. The probe pulse was split into two by a neutral density filter. One portion of the probe pulse served as the reference and was directly sent to the fiber-optic coupled multichannel spectrometers (CCD and InGaAs sensors). The rest of the probe pulse together with the pump pulse were focused onto the same spot on the samples with a beam size of around 0.5 mm^2 before sending it to the spectrometer.

Carrier-selective photo-CELIV measurement

A synchronized setup, consisting of pulsed Nd:YAG laser (OPOTEK, VIBRANT 355 LD, with a repetition rate of 10 Hz and a pulse width of 5 ns) was synchronized with an arbitrary function generator (Agilent 33220A) and a delay time generator (Quantum Composers 9520), was utilized for photo-CELIV measurements and the data were collected using an oscilloscope (Agilent DSO3202A). Here, the actual device architecture was used for measurement including an additional 10 nm of Al_2O_3 layer (deposited by radio-frequency magnetron sputtering) to separate the PNC active layer from either cathode or anode.^[39] This allows a single carrier (i.e., holes or electrons) transport across the system, enabling selective assessments for each charge carrier. A ramp-like voltage pulse with an acceleration rate of 1.5 V (or 1.7 V) / 15 μs for hole

(or electron) extraction was employed and a fixed offset voltage of -1.0 V was applied to compensate the built-in potential established in the device system.

The carrier mobility values were estimated from the timepoint at the peak of transients (t_{max}) based on the equation modified by Lorrman *et al.*^[48]:

$$\mu = \frac{d^2}{2At_{max}^2} \left[\frac{1}{6.2 \left(1 + 0.002 \frac{\Delta J}{J_0}\right)} + \frac{1}{\left(1 + 0.12 \frac{\Delta J}{J_0}\right)} \right]^2$$

where ΔJ , J_0 , A , and d correspond to the difference between the maximum current transient and the dark current, displacement current, ramp rate of the extraction pulse, and sample thickness, respectively.^[39, 49-51] A mobility value averaged over the delay time range was denoted as $\langle \mu \rangle$ and regarded as a representative value for the mobility of each PNC system.^[39, 44]

The recombination lifetime (τ_B) were estimated from the extracted hole concentrations in each device by integrating the photocurrent transient with time at each delay time. These values plotted as a function of the delay time can be expressed by the following Langevin recombination model:

$$e(t) \text{ (or } p(t)) = \frac{e_0 \text{ (or } p_0)}{1 + \left(\frac{t}{\tau_B}\right)}$$

where $e(t)$ (or $p(t)$), e_0 (or p_0), and τ_B correspond to the electron (hole) concentration after the corresponding delay time, initial electron (hole) concentration, and bimolecular recombination lifetime, respectively.^[39, 40]

The diffusion lengths (L_{DS}) of charge carriers were estimated according to the following equation based on the mobility-time product (Einstein relationship):

$$L_D = \sqrt{(kT/q) \times \mu \tau}$$

where k is the Boltzmann constant, T is the temperature (300 K), and q is the elemental charge. For calculations, the values of $\langle \mu \rangle$ and τ_B , obtained from photo-CELIV measurements, were respectively substituted to μ and τ in the equation, which produces comparable L_{DS} with previous reports.^[39, 44]

Computational details

All *ab initio* calculations were performed with the Vienna Ab initio Simulation Package (VASP) 5.4.4.^[52-55] The Projector Augmented Wave (PAW) method^[55-57] was employed and exchange-correlation interactions were treated by means of Perdew-Burke-Ernzerhof (PBE)^[58] functional under the generalized gradient approximation (GGA). We used Gamma-centered k -points mesh $2 \times 2 \times 1$ in each primitive lattice vector of the reciprocal space for geometric optimization.^[59] DFT-D3 dispersion correction was used to take vdW interaction into account.^[58-60] A plane-wave cutoff energy of 500 eV was used. Lattice constants and internal atomic positions were fully optimized until the residual forces were less than 0.04 eV/Å. Geometric details of the slab model and binding, solvation tendency of ligands to the CsPbI₃ by DFT simulations are explained in **Supplementary Note 1 and 2**. Also, water penetration simulations by molecular dynamics are explained in **Supplementary Note 3**.

References

- [1] Akkerman, Q. A., Raino, G., Kovalenko, M. V. & Manna, L. Genesis, challenges and opportunities for colloidal lead halide perovskite nanocrystals. *Nat. Mater.* **17**, 394–405 (2018).
- [2] Khan, J. et al. Hybrid quantum dot/organic heterojunction: a route to improve open-circuit voltage in PbS colloidal quantum dot solar cells. *ACS Energy Lett.* **5**, 3322–3329 (2020).
- [3] Kim, J. et al. Hydrophobic stabilizer-anchored fully inorganic perovskite quantum dots enhance moisture resistance and photovoltaic performance. *Nano Energy* **75**, 104985 (2020).
- [4] Ling, X. F. et al. 14.1% CsPbI₃ perovskite quantum dot solar cells via cesium cation passivation. *Adv. Energy Mater.* **9**, 1900721 (2019).
- [5] Pan, J. et al. Bidentate ligand-passivated CsPbI₃ perovskite nanocrystals for stable near-unity photoluminescence quantum yield and efficient red light-emitting diodes. *J. Am. Chem. Soc.* **140**, 562–565 (2018).
- [6] Protesescu, L. et al. Nanocrystals of cesium lead halide perovskites (CsPbX₃, X = Cl, Br, and I): novel optoelectronic materials showing bright emission with wide color gamut. *Nano Lett.* **15**, 3692–3696 (2015).
- [7] Song, J. Z. et al. Quantum dot light-emitting diodes based on inorganic perovskite cesium lead halide (CsPbX₃). *Adv. Mater.* **27**, 7162–7167 (2015).
- [8] Swarnkar, A. et al. Quantum dot-induced phase stabilization of α -CsPbI₃ perovskite for high-efficiency photovoltaics. *Science*, **354**, 92–95 (2016).

- [9] Wang, Y. et al. Surface ligand management aided by a secondary amine enables increased synthesis yield of CsPbI₃ perovskite quantum dots and high photovoltaic performance. *Adv. Mater.* **32**, 2000449 (2020).
- [10] Yuan, J. et al. Metal halide perovskites in quantum dot solar cells: progress and prospects. *Joule* **4**, 1160–1185 (2020).
- [11] Conings, B. et al. Intrinsic thermal instability of methylammonium lead trihalide perovskite. *Adv. Energy Mater.* **5**, 1500477 (2015).
- [12] Han, B. N. et al. Stable, efficient red perovskite light-emitting diodes by (α , δ)-CsPbI₃ phase engineering. *Adv. Funct. Mater.* **28**, 1804285 (2018).
- [13] Dong Y. T. et al. Bipolar-shell resurfacing for blue LEDs based on strongly confined perovskite quantum dots. *Nat. Nanotechnol.* **15**, 668–674 (2020).
- [14] Li, J. et al. 50-fold EQE improvement up to 6.27% of solution-processed all-inorganic perovskite CsPbBr₃ QLEDs via surface ligand density control. *Adv. Mater.* **29**, 1603885 (2017).
- [15] Pan, J. et al. Highly efficient perovskite-quantum-dot light-emitting diodes by surface engineering. *Adv. Mater.* **28**, 8718–8725 (2016).
- [16] Xue, J. J. et al. Surface ligand management for stable FAPbI₃ perovskite quantum dot solar cells. *Joule*, **2**, 1866–1878 (2018).
- [17] Wheeler, L. M. et al. Targeted ligand-exchange chemistry on cesium lead halide perovskite quantum dots for high-efficiency photovoltaics. *J. Am. Chem. Soc.* **140**, 10504–10513 (2018).
- [18] Zhao, Q. et al. High-efficiency perovskite quantum dot solar cells with charge separating heterostructure. *Nat. Commun.* **10**, 2842 (2019).
- [19] Sanehira, E. M. et al. Enhanced mobility CsPbI₃ quantum dot arrays for record-efficiency, high-voltage photovoltaic cells. *Sci. Adv.* **3**, eaao4204 (2017).
- [20] Chiba, T. et al. High-efficiency perovskite quantum-dot light-emitting devices by effective washing process and interfacial energy level alignment. *ACS Appl. Mater. Interfaces* **9**, 18054–18060 (2017).
- [21] De Roo, J. et al. Highly dynamic ligand binding and light absorption coefficient of cesium lead bromide perovskite nanocrystals. *ACS Nano* **10**, 2071–2081 (2016).
- [22] Hao, M. et al. Ligand-assisted cation-exchange engineering for high-efficiency colloidal Cs_{1-x}FA_xPbI₃ quantum dot solar cells with reduced phase segregation. *Nat. Energy* **5**, 79–88 (2020).
- [23] Hoshi, K. et al. Purification of perovskite quantum dots using low-dielectric-constant washing solvent “diglyme” for highly efficient light-emitting devices. *ACS Appl. Mater. Interfaces* **10**, 24607–24612 (2018).
- [24] Thomas, C. J. et al. Thermal stability of the black perovskite phase in cesium lead iodide

- nanocrystals under humid conditions. *Chem. Mater.* **31**, 9750–9758 (2019).
- [25] Lee, S. et al. Orthogonal colloidal quantum dot inks enable efficient multilayer optoelectronic devices. *Nat. Commun.* **11**, 4814, (2020).
- [26] Suh, Y.-H., Kim, T., Choi, J. W., Lee, C. L. & Park, J. High-performance CsPbX₃ perovskite quantum-dot light-emitting devices via solid-state ligand exchange. *ACS Appl. Nano Mater.* **1**, 488–496 (2018).
- [27] Li, F. et al. Postsynthetic surface trap removal of CsPbX₃ (X = Cl, Br, or I) quantum dots via a ZnX₂/hexane solution toward an enhanced luminescence quantum yield. *Chem. Mater.* **30**, 8546–8554 (2018).
- [28] Zhang, L. et al. All-inorganic CsPbI₃ quantum dot solar cells with efficiency over 16% by defect control. *Adv. Funct. Mater.* **31**, 2005930 (2021).
- [29] Grisorio, R. et al. Exploring the surface chemistry of cesium lead halide perovskite nanocrystals. *Nanoscale* **11**, 986–999 (2019).
- [30] Chiba, T. et al. Anion-exchange red perovskite quantum dots with ammonium iodine salts for highly efficient light-emitting devices. *Nat. Photon.* **12**, 681–687 (2018).
- [31] Vickers E. T. et al. Enhancing charge carrier delocalization in perovskite quantum dot solids with energetically aligned conjugated capping ligands *ACS Energy Lett.* **5**, 817–825 (2020).
- [32] Vickers, E. T. et al. T. A. Graham, A. H. Chowdhury, B. Bahrami, B. W. Dreskin, S. Lindley, S. B. Naghadeh, Q. Q. Qiao and J. Z. Zhang, *ACS Energy Lett.*, 2018, **3**, 2931–2939.
- [33] E. T. Vickers, Ligand dependent growth and optical properties of hybrid organo-metal halide perovskite magic sized clusters. *J. Phys. Chem. C*, **123**, 18746–18752 (2019).
- [34] Jia, D. et al. Surface matrix curing of inorganic CsPbI₃ perovskite quantum dots for solar cells with efficiency over 16%. *Energy Environ. Sci.* **14**, 4599–4609 (2021).
- [35] Jeong, W. H. et al. In situ cadmium surface passivation of perovskite nanocrystals for blue LEDs. *J. Mater. Chem. A* **9**, 26750–26757 (2021).
- [36] Lee, S. et al. Amine-based passivating materials for enhanced optical properties and performance of organic-inorganic perovskites in light-emitting diodes. *J. Phys. Chem. Lett.* **8**, 1784–1792 (2017).
- [37] Fassel, P. et al. Fractional deviations in precursor stoichiometry dictate the properties, performance and stability of perovskite photovoltaic devices. *Energy Environ. Sci.* **11**, 3380–3391 (2018).
- [38] Ling, X. et al. Guanidinium-assisted surface matrix engineering for highly efficient perovskite quantum dot photovoltaics. *Adv. Mater.* **32**, 2001906 (2020).
- [39] Yang, J., Lee, J., Lee, J. & Yi, W. Improving charge collection from colloidal quantum dot photovoltaics by single-walled carbon nanotube incorporation. *ACS Appl. Mater.*

- Interfaces*, **11**, 33759–33769 (2019).
- [40] Yang, J. et al. Guanidinium-pseudohalide perovskite interfaces enable surface reconstruction of colloidal quantum dots for efficient and stable photovoltaics. *ACS Nano* **16**, 1649–1660 (2022).
- [41] Petrovic, M., Ye, T., Vijila, C. & Ramakrishna, S. Influence of charge transport and defect on the performance of planar and mesostructured perovskite solar cells. *Adv. Energy Mater.* **7**, 1602610 (2017).
- [42] Musilenko, A. et al. Deciphering the effect of traps on electronic charge transport properties of methylammonium lead tribromide perovskite. *Sci. Adv.* **6**, eabb6393 (2020).
- [43] Jin, H. et al. It’s a trap! On the nature of localised states and charge trapping in lead halide perovskites. *Mater. Horiz.* **7**, 397–410 (2020).
- [44] Yang, J. et al. Solvent engineering of colloidal quantum dot inks for scalable fabrication of photovoltaics. *ACS Appl. Mater. Interfaces.* **13**, 36992–37003 (2021).
- [45] Hu, L. et al. Flexible and efficient perovskite quantum dot solar cells via hybrid interfacial architecture. *Nat. Commun.* **12**, 466 (2021).
- [46] Xue, J. et al. A small-molecule “charge driver” enables perovskite quantum dot solar cells with efficiency approaching 13%. *Adv. Mater.* **31**, 1900111 (2019).
- [47] Yang, J. et al. Hybrid surface passivation for retrieving charge collection efficiency of colloidal quantum dot photovoltaics. *ACS Appl. Mater. Interfaces* **12**, 43576–43585 (2020).
- [48] Lorrmann, J., Badada, B. H., Imganas, O., Dyakonov, V. & Diebel, C. Charge carrier extraction by linearly increasing voltage: analytic framework and ambipolar transients. *J. Appl. Phys.* **108**, 113705 (2010).
- [49] Mozer, A. J. et al. Time-dependent mobility and recombination of the photoinduced charge carriers in conjugated polymer/fullerene bulk heterojunction solar cells. *Phys. Rev. B* **72**, 035217 (2005).
- [50] Mozer, A. J. et al. Charge transport and recombination in bulk heterojunction solar cells studied by the photoinduced charge extraction in linearly increasing voltage technique. *Appl. Phys. Lett.* **86**, 112104 (2005).
- [51] Juska, G., Arlauskas, K., Viliunas, M., Kocka, J. Extraction current transients: new method of study of charge transport in microcrystalline silicon. *Phys. Rev. Lett.* **84**, 4946–4949 (2000).
- [52] Kresse, G. & Hafner, J. *Ab initio* molecular dynamics for open-shell transient metals. *Phys. Rev. B* **48**, 13115–13118 (1993).
- [53] Kresse, G. & Hafner, J. *Ab initio* molecular-dynamics simulation of the liquid-metal–amorphous-semiconductor transition in germanium. *Phys. Rev. B*, 1994, **49**, 14251–

14269.

- [54] Kresse, G. & Furthmuller, J. Efficiency of ab-initio total energy calculations for metals and semiconductors using a plane-wave basis set. *Comput. Mater. Sci.* **6**, 15–50 (1996).
- [55] Kresse, G. & Furthmuller, J. Efficient iterative schemes for *ab initio* total-energy calculations using a plane-wave basis set. *Phys. Rev. B* **54**, 11169-11186 (1996).
- [56] Blochl, P. E. Projector augmented-wave method. *Phys. Rev. B* **50**, 17953–17979 (1994).
- [57] Kresse, G. & Joubert, D. From ultrasoft pseudopotentials to the projector augmented-wave method. *Phys. Rev. B* **59**, 1758–1775 (1999).
- [58] J. P. Perdew, K. Burke, M. Ernzerhof, Generalized gradient approximation made simple. *Phys. Rev. Lett.* **77**, 3865-3868 (1996).
- [59] Monkhorst, H. J. & Pack, J. D. Special points for Brillouin-zone integrations. *Phys. Rev. B* **13**, 5188–5192 (1976).
- [60] Grimme, S., Antony, J., Ehrlich, S. & Krieg, H. A consistent and accurate *ab initio* parametrization of density functional dispersion correction (DFT-D) for the 94 elements H-Pu. *J. Chem. Phys.* **132**, 154104 (2010).

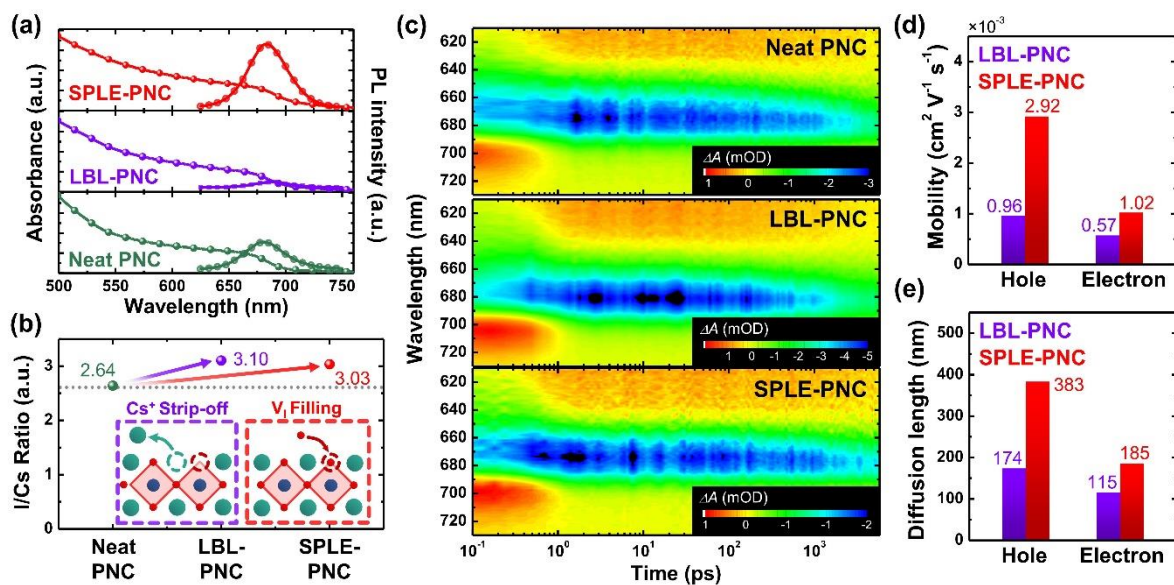


Figure 2. (a) Absorption and PL spectra of the PNC films. (b) Estimated I to Cs elemental ratio of the PNC films, based on XPS analysis. (c) fs-TA spectro-temporal maps of the PNC films. The pump wavelength was 380 nm (fluence: 2.5 nJ cm⁻²) Estimated (d) mobility and (e) diffusion lengths (for electrons and holes) of LBL- and SPLE-PNC matrices based on photo-CELIV analysis.

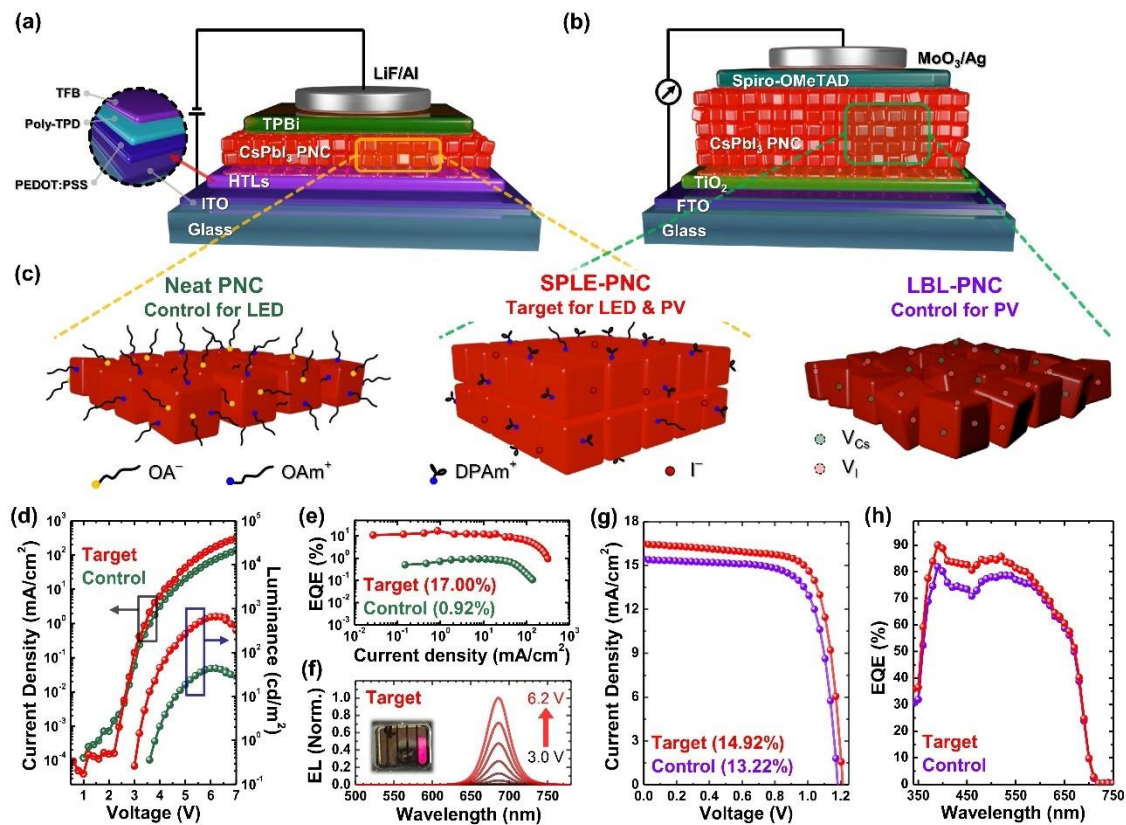


Figure 3. Schematics depicting the respective device architectures of PNC-based (a) LED and (b) PV, and (c) corresponding PNC matrices that are employed as an emissive layer and active layer for LED and PV, respectively. (d) J - V - L , and (e) EQE curves of the LED devices, respectively. (g) EL spectra of target LED. (g) J - V curves and (h) EQE spectra of the PV devices, respectively.

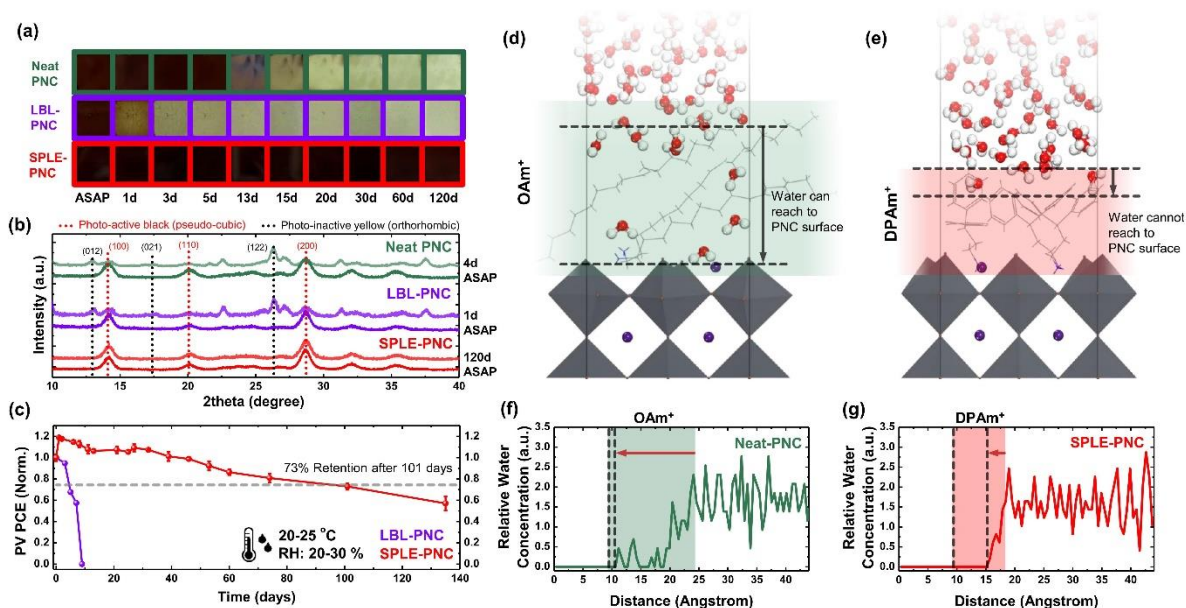


Figure 4. (a) Time-series images of the PNC films under ambient storage conditions. (b) XRD patterns of the fresh and aged PNC films for each preparation method. (c) Evolution of PV PCEs as a function of ambient storage times. Snapshots of (d) OAm⁺ and (e) DPAm⁺-capped PNC surfaces exposed to water based on MD simulations. Relative concentrations of water molecules present in the vicinity of (f) OAm⁺ and (g) DPAm⁺-capped PNC surfaces. The results suggest that DPAm⁺ provides an effective barrier to water penetration into the PNC lattices, in contrast to OAm⁺ ligands.

Table 1. Summarized performances of the champion PNC optoelectronics

Sample configuration	LED (Control: Neat PNC)				PV (Control: LBL-PNC)			
	L_{\max} (cd/m ²) @bias	EQE _{peak} (%) @bias	V_{TO} (V)	EL peak wavelength (nm)	V_{oc} (V)	J_{sc} (mA/cm ²)	FF (%)	PCE (%)
Control	43.67@6.0	0.92@4.4	3.4	681	1.18	15.39	72.77	13.22
Target (SPLE-PNC)	656.5@6.0	17.00@3.4	2.8	684	1.21	16.64	73.89	14.92

Supplementary Information

A universal perovskite nanocrystal ink for high-performance optoelectronic devices

Hochan Song^{1,†}, Jonghee Yang^{2,†}, Woo Hyeon Jeong^{1,†}, Jeongjae Lee^{3,†}, Tack Ho Lee⁴,
Jung Won Yoon¹, Hajin Lee⁵, Alexandra J. Ramadan⁶, Robert D. J. Oliver⁶,
Seong Chan Cho⁵, Seul Gi Lim¹, Ji Won Jang¹, Zhongkai Yu⁷, Jae Taek Oh¹, Eui Dae Jung⁸,
Myoung Hoon Song⁸, Sung Heum Park⁷, James R. Durrant⁴,
Henry. J. Snaith⁶, Sang Uck Lee⁵, Bo Ram Lee^{7,*} and Hyosung Choi^{1,*}

¹Department of Chemistry, Research Institute for Convergence of Basic Sciences, and Research Institute for Natural Science, Hanyang University, Seoul 04763, Republic of Korea

²Institute for Advanced Materials and Manufacturing, Department of Materials Science and Engineering, University of Tennessee, Knoxville, TN 37996, United States

³School of Earth and Environmental Sciences, Seoul National University Seoul 08826, Republic of Korea

⁴Department of Chemistry and Centre for Processable Electronics, Imperial College London, London W12 0BZ, United Kingdom

⁵Department of Applied Chemistry, Center for Bionano Intelligence Education and Research, Hanyang University, Ansan 15588, Republic of Korea

⁶Department of Physics, University of Oxford, Clarendon Laboratory, Parks Road, Oxford, OX1 3PU, United Kingdom

⁷Department of Physics, Pukyong National University, Busan 608-737, Republic of Korea

⁸Department of Materials Science and Engineering, Ulsan National Institute of Science and Technology (UNIST), Ulsan 44919, Republic of Korea

[†]These authors contributed equally: Hochan Song, Jonghee Yang, Woo Hyeon Jeong, Jeongjae Lee.

*e-mail: brlee@pknu.ac.kr; hschoi202@hanyang.ac.kr

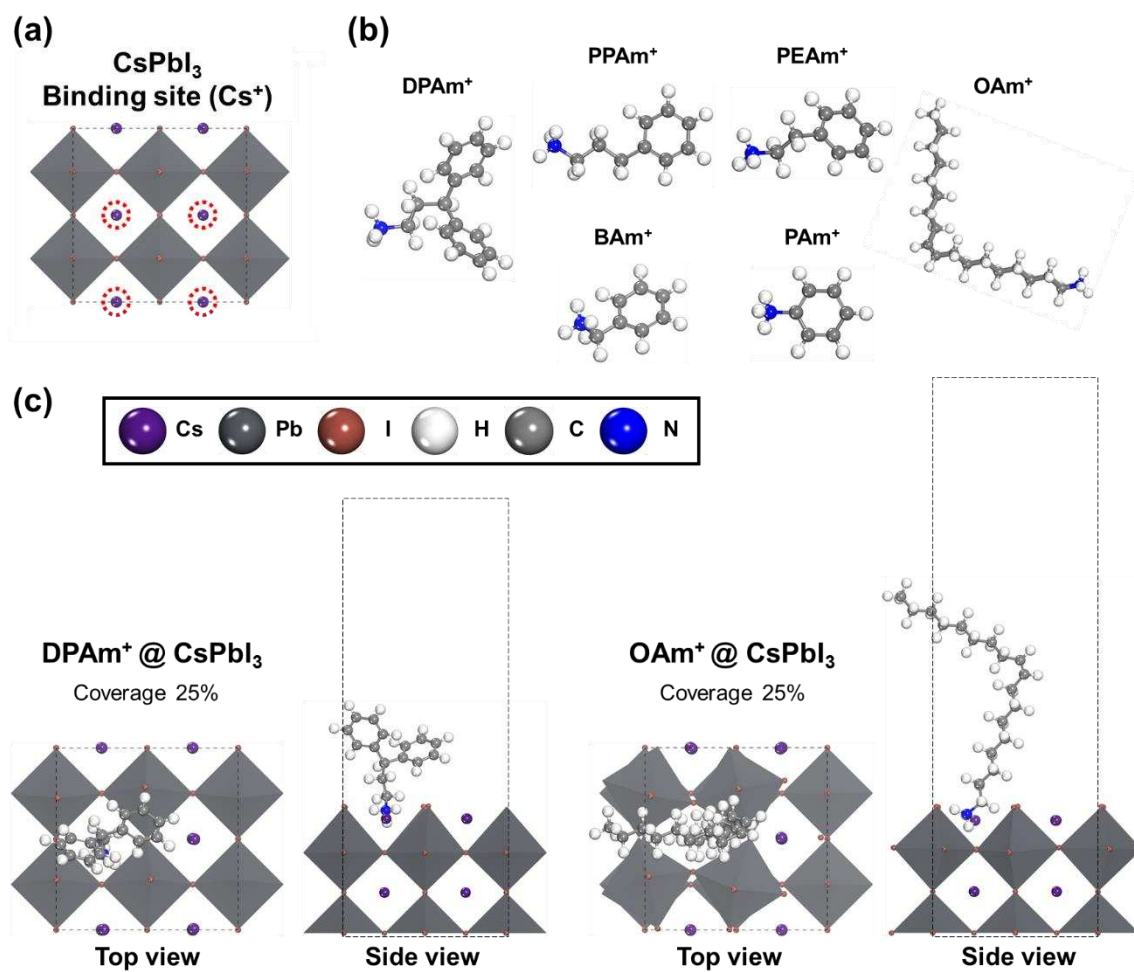
Supplementary Note 1. CsPbI₃ surface slab modeling and binding energy details.

Herein, we systematically designed the CsPbI₃ surface slab models to perform DFT simulations. Since the ligand exchange process for the CsPbI₃ PNC means changing the Cs atom to the ligand, we used only the Cs-terminated surface models. Then, we considered the slab model of the CsPbI₃ (100) surface with 4 layers (2×2 unit cell). To mimic the bulk properties of CsPbI₃, we set the bottom 2 layers of CsPbI₃ (100) are fixed. The CsPbI₃ surface slab models have vacuum space in the *z*-direction that was set to 15 Å to avoid interactions between layers. In addition, we consider the binding configuration and orientation of organic ligands, which are likely to provide strong van der Waals interactions with CsPbI₃ perovskite (**Supplementary Fig. 1**).

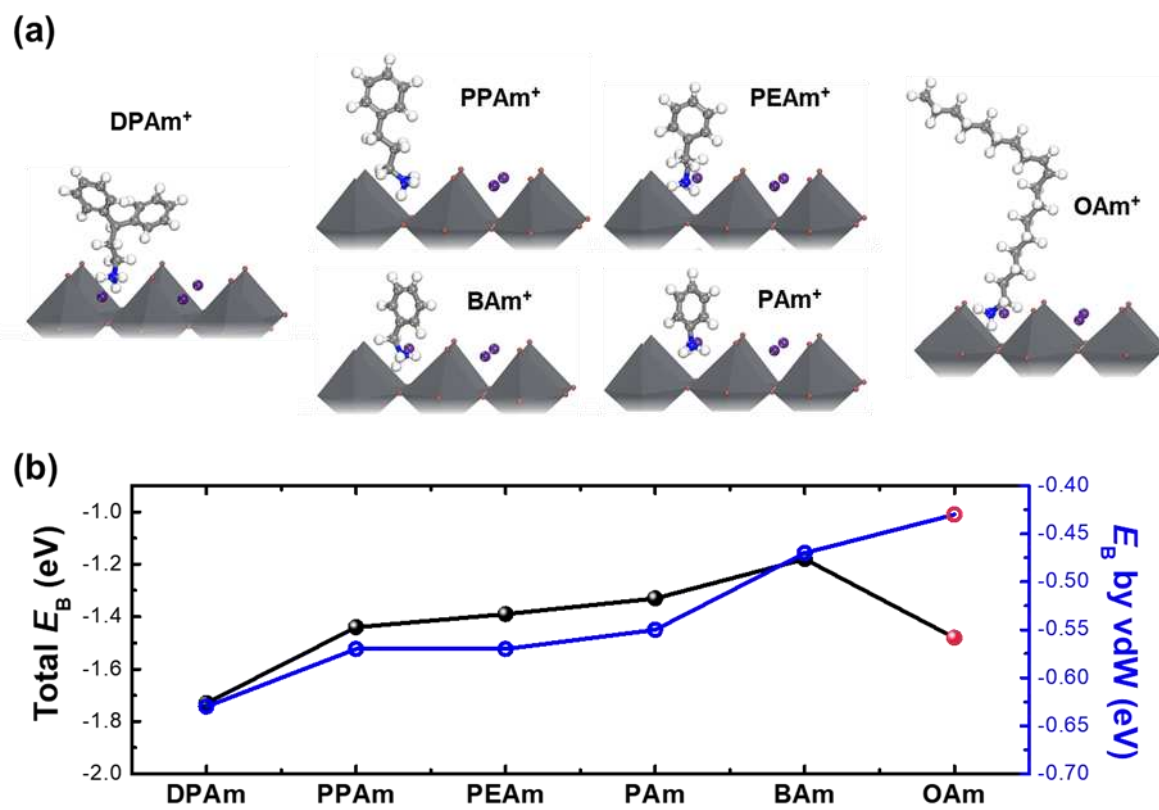
To investigate the interaction between organic ligands and CsPbI₃ surface, we calculated the binding energy (ΔE_b), which is explained in the following equation,

$$\Delta E_b = E_{\text{ligand}^*@\text{CsPbI}_3} + E_{\text{Cs}} - (E_{\text{CsPbI}_3} + E_{\text{ligand}}) \quad (\text{eq. 1})$$

where $E_{\text{ligand}^*@\text{CsPbI}_3}$ is the total energy of the ligand adsorbate CsPbI₃ surface, E_{CsPbI_3} is the total energy of the pure CsPbI₃ surface and E_{ligand} is the total energy of each ligand (DPAm⁺, PPA⁺, PEAm⁺, BA⁺, PAm⁺, OAm⁺), and E_{Cs} is the Cs total energy of bulk/atom. The negative value of the total binding energy means that the ligand binding to the CsPbI₃ surface is thermodynamically favorable. Additionally, in order to investigate the effect of non-bond interaction on the ligand binding, we compare the total binding energy (ΔE_b) with and without van der Waals (vdW) contribution. (**Supplementary Fig. 2**).



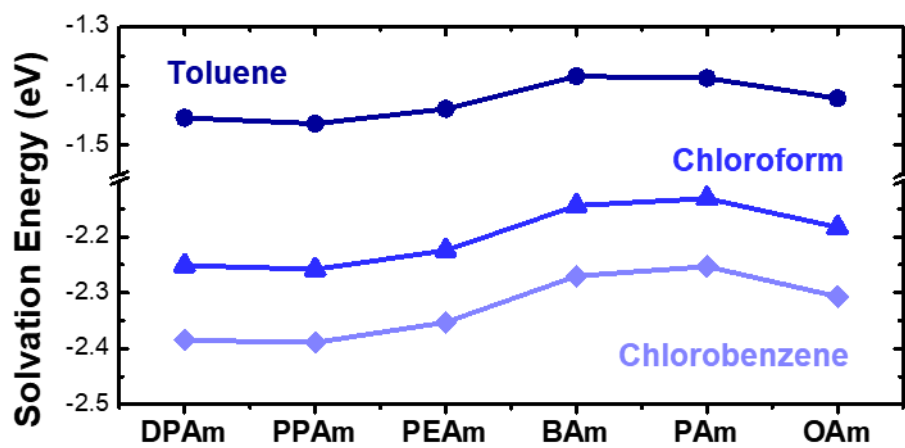
Supplementary Fig. 1. (a) Ligand binding sites of CsPbI₃ surface (the red circle corresponding to the V_{Cs} and ligand binding site). (b) aromatic ligand structures used for the total binding energy and solvation energy. (c) top view and side view of the DPAm⁺ and OAm⁺ at the CsPbI₃ surfaces.



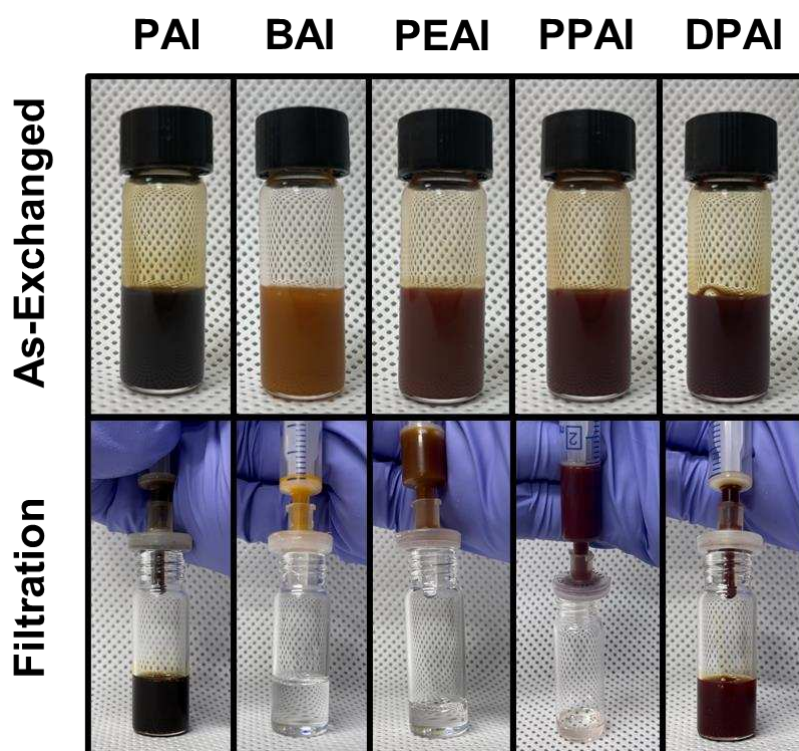
Supplementary Fig. 2. Binding affinities of aromatic ligands.

Supplementary Note 2. Solvation energy with the COSMO method.

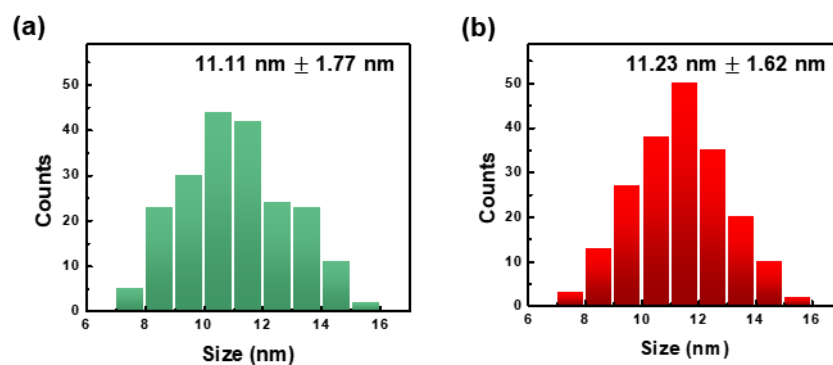
To unveil the solvation energy of the ligand@CsPbI₃ surface with various solvents (Toluene, Chloroform, Chlorobenzene), we use the COSMO module of DMol³ code^[1,2] in Material Studio 2020 (BIOVIA, San Diego, CA), which is basically based on density functional theory. In DMol3, the electronic wave function was expanded in a localized atom-centered basis set with each basis function defined numerically on a dense radial grid. We used the double-numeric polarized (DND) basis sets.^[1,2] The electron exchange and correlation interaction were analyzed by the generalized gradient approximation (GGA) with Perdew-Burke-Ernzerhof (PBE) functional method. The COSMO method used the continuum solvation ‘Conductor-like Screening Model’ method to describe specific dielectric screening effects in a solvent.^[3,4] The solvation energies were shown in **Supplementary Fig. 3.**, it indicated the additional stability of ligand@CsPbI₃ surface by various solvents, which aid to the expects the dispersion of ligand with solvents.



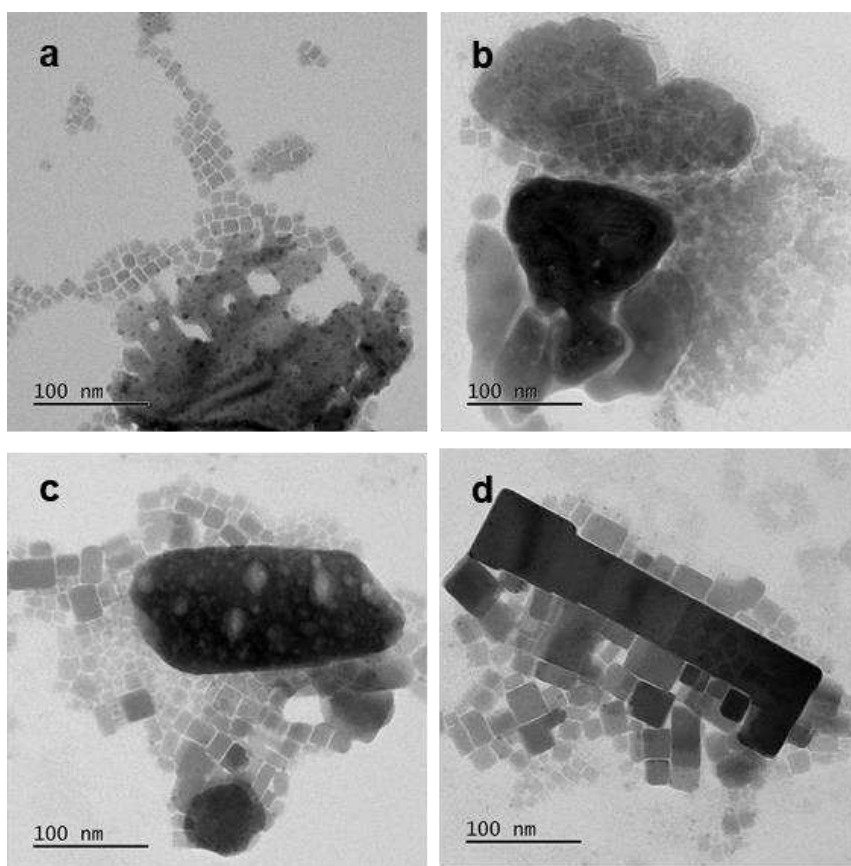
Supplementary Fig. 3. Solvation energies (in various solvents) of the aromatic cations considered in this study.



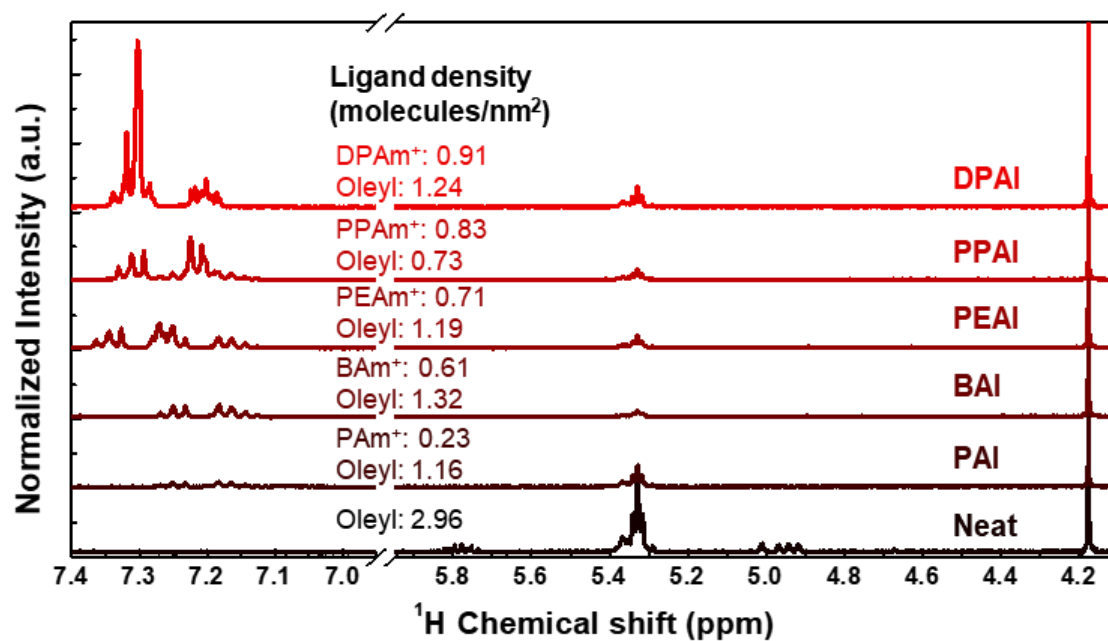
Supplementary Fig. 4. Photographs showing concentrated (150 mg mL^{-1}) colloidal dispersion of the SPLE-PNCs. Only the SPLE-PNC prepared with DPAI could pass through the syringe filter (pore size of $0.22 \mu\text{m}$), indicating that the other ligands experienced severe aggregations and/or fusion. Note that the use of PAI cannot initiate SPLE, in accordance with previous report.^[5] That is, the filtered dispersion is OA-PNC.



Supplementary Fig. 5. Histograms for size distributions of (a) neat and (b) SPLE-PNCs, according to the collected TEM images. The results indicate that the solution phase ligand exchange by using DPAI does not compromise original PNC dimensionality.

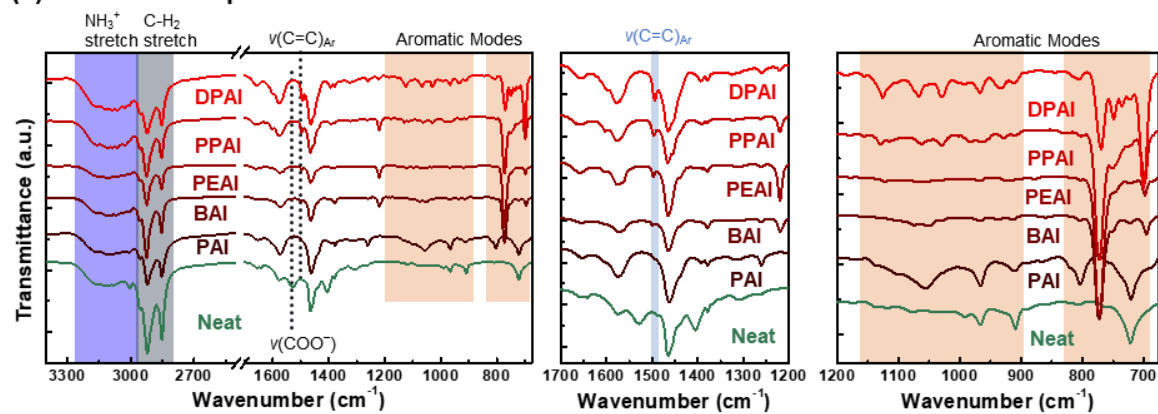


Supplementary Fig. 6. (a and b) TEM images of SPLE-PNCs using PEAI, collected from two different spots. Both images clearly exhibit merged features, responsible for insufficient ligand exchange and consequent poor surface management.

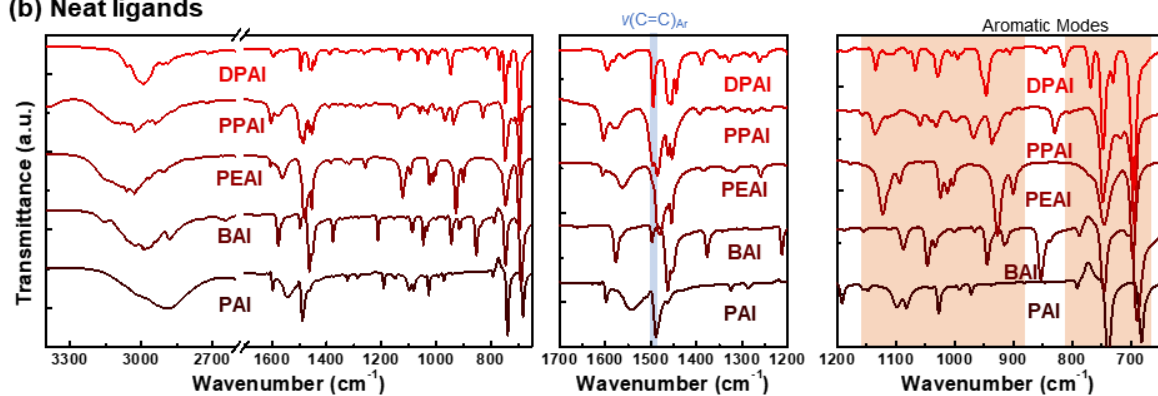


Supplementary Fig. 7. ¹H NMR spectra of the SPLE-PNCs upon dissolution in DMSO-*d*₆. A fixed concentration of ferrocene was incorporated into the solution as an internal standard. This allows us to quantify the exact densities of the ligands for a fixed size (10 nm edge) of cubic-shaped PNCs.

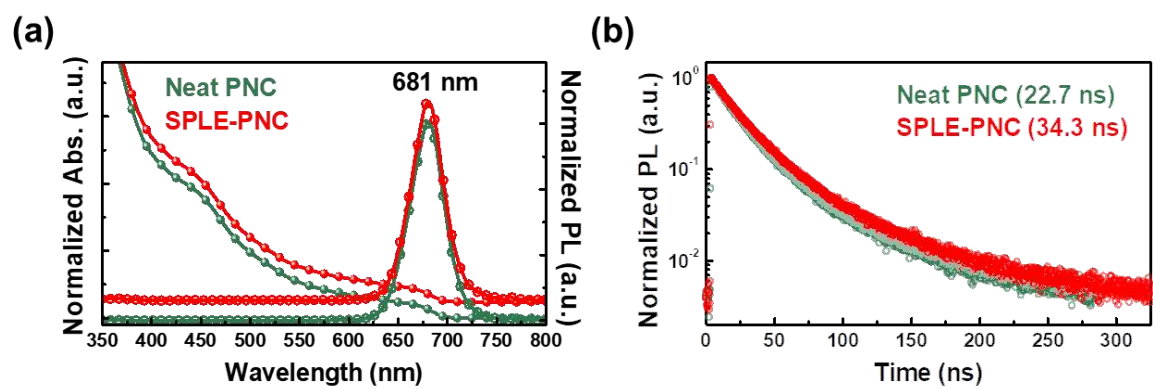
(a) SPLE-PNC dispersions



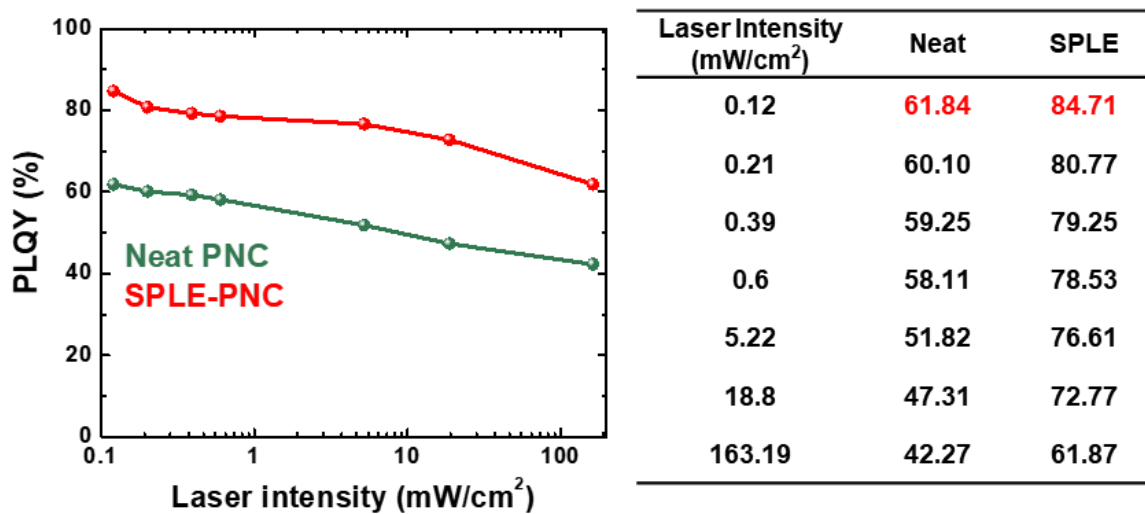
(b) Neat ligands



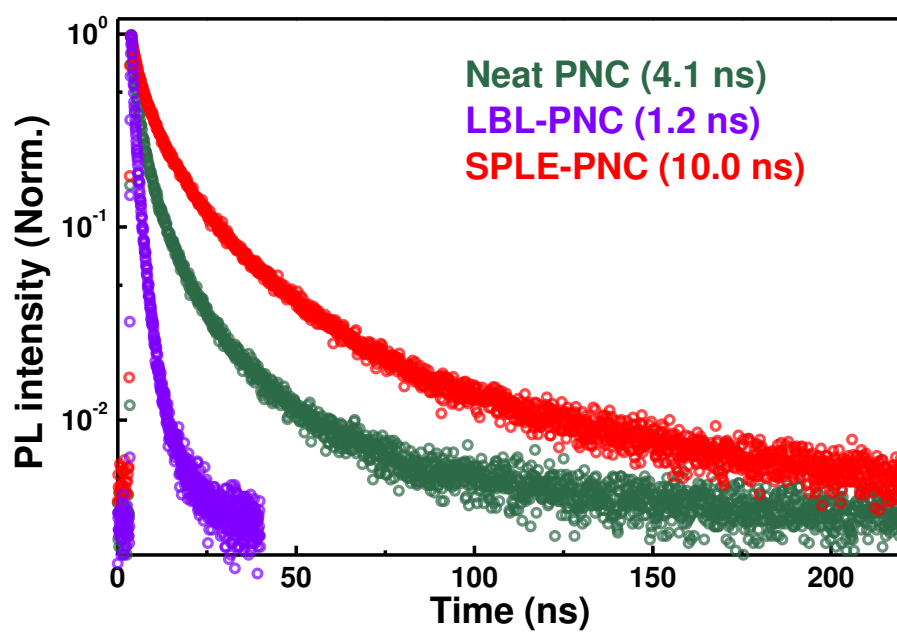
Supplementary Fig. 8. FTIR spectra of (a) SPLE-PNC films and (b) neat ligands.



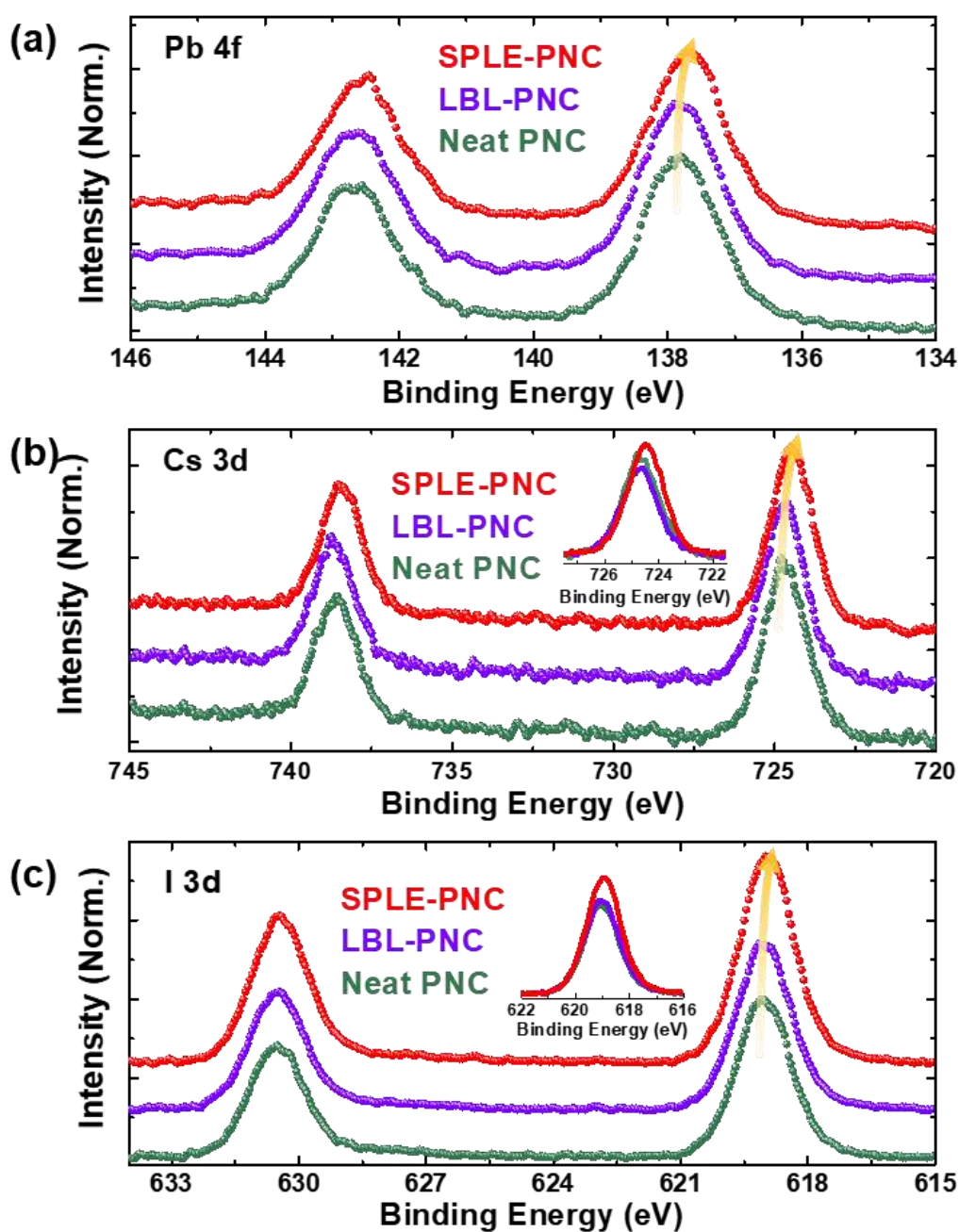
Supplementary Fig. 9. (a) Normalized absorption and PL spectra of the PNC dispersions. (b) Time-resolved PL decay curves of the PNC dispersions.



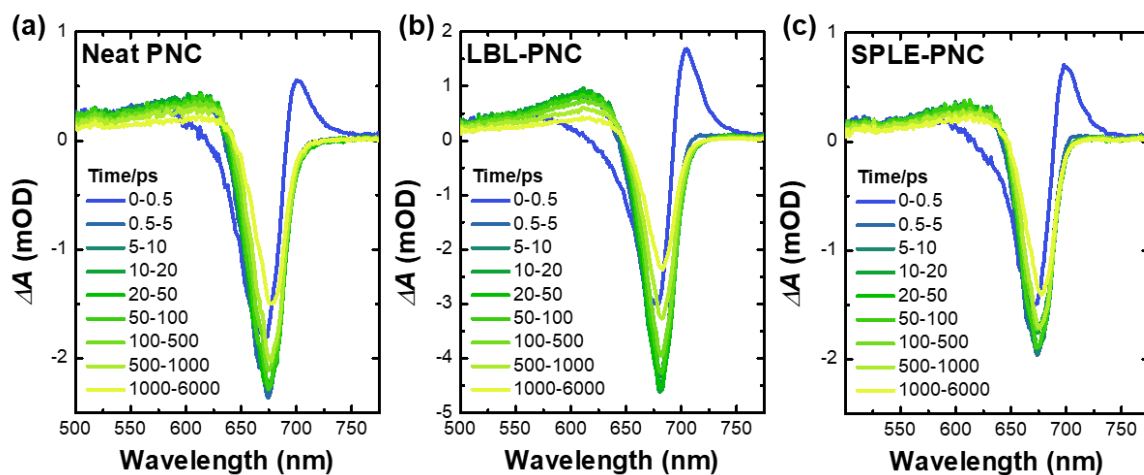
Supplementary Fig. 10. Laser fluence-dependent PLQY of the PNC films. Note that LBL-PNC film produced negligible PL response upon laser excitation and therefore, PLQYs could not be measured.



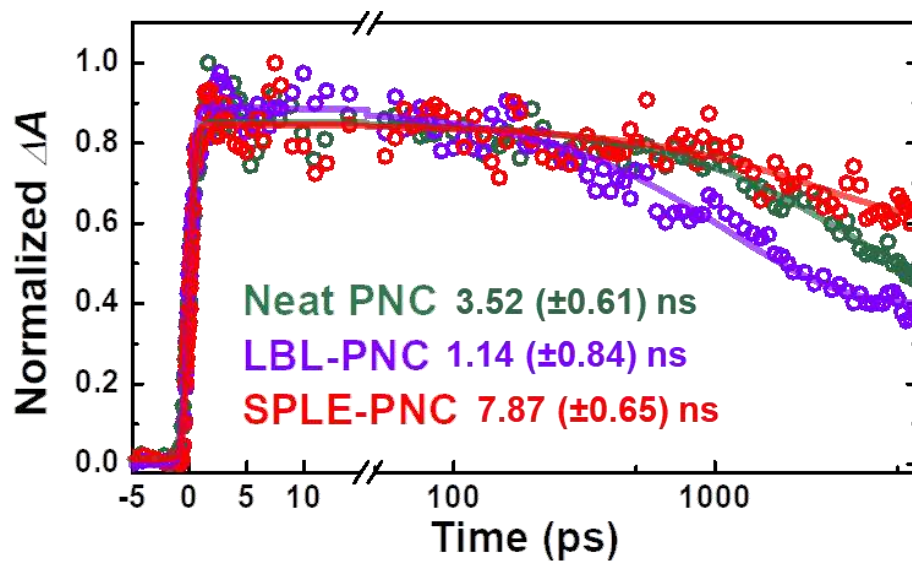
Supplementary Fig. 11. TRPL decay curves of the PNC films.



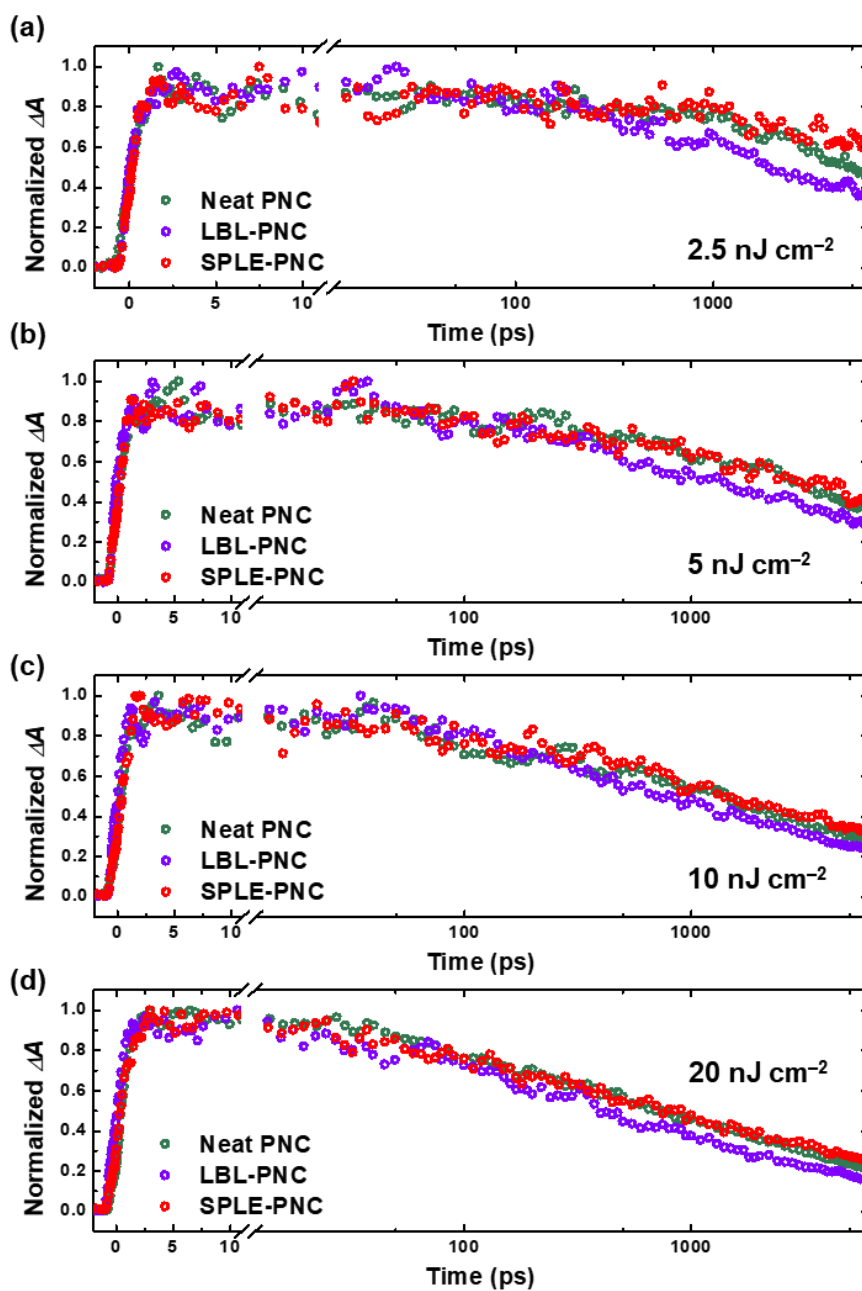
Supplementary Fig. 12. XPS (a) Pb 4f, (b) Cs 3d, and (c) I 3d core-level spectra of the PNC films. The insets reveal the relative differences (normalized by Pb 4f intensity of each film) in intensity of the photoemission peaks, responsible for the actual level of the element (associated with surface passivation) in the PNCs.



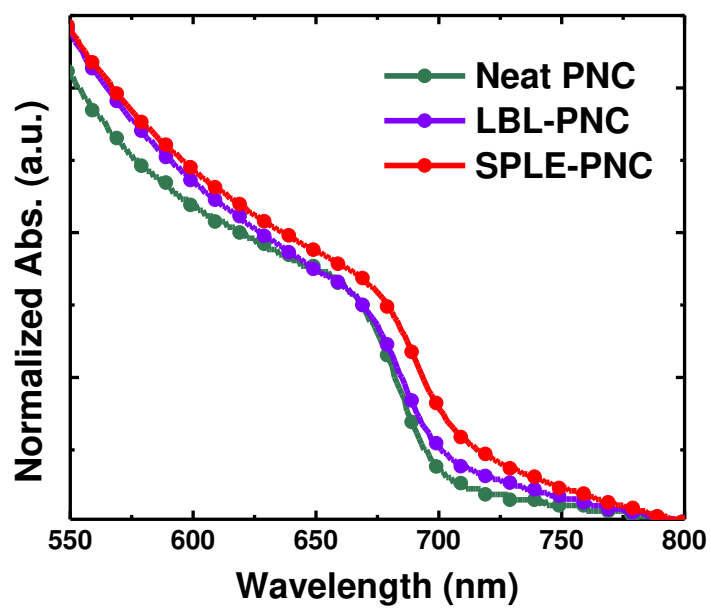
Supplementary Fig. 13. fs-TA spectra of the PNC films averaged over different range of time delays. The pump wavelength was 380 nm (fluence: 2.5 nJ cm^{-2}).



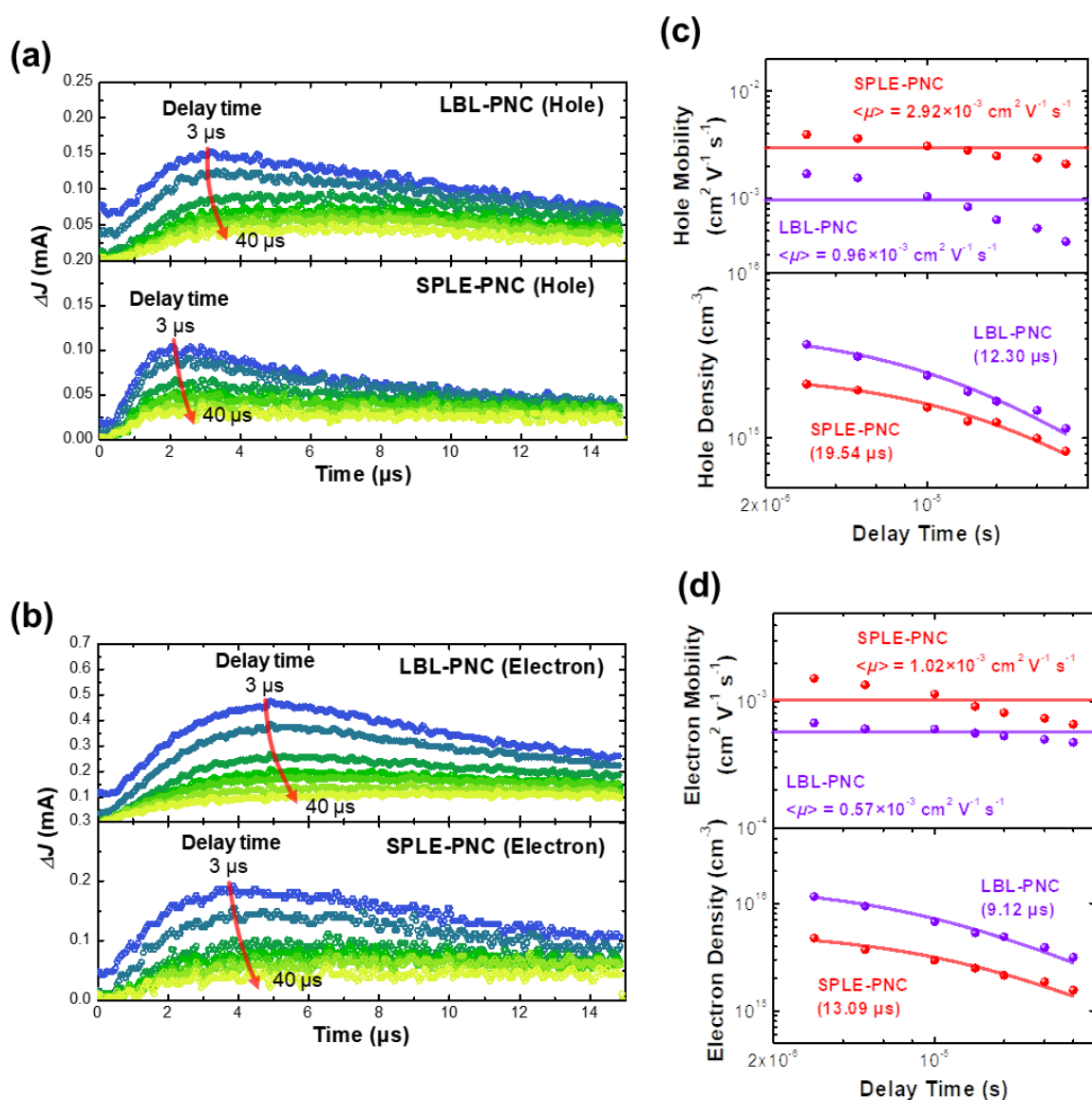
Supplementary Fig. 14. Normalized GSB decay curves of the PNCs at the wavelength region probed from 675~685 nm (the band-edge position).



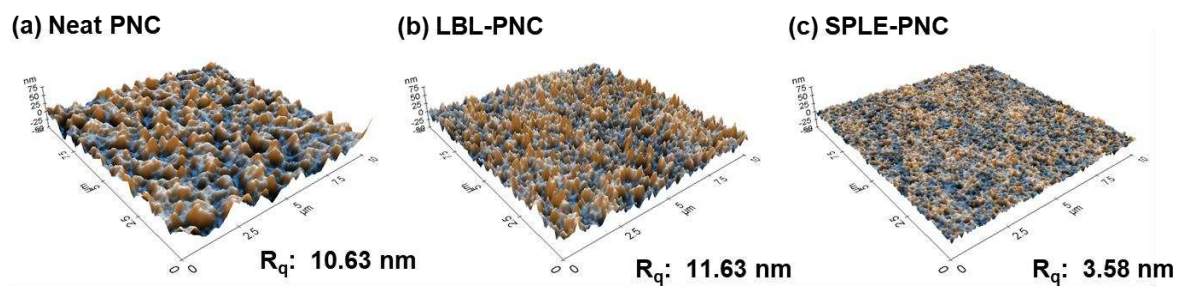
Supplementary Fig. 15. GSB decay curves of the PNCs (probed at 675~685 nm) from fs-TA measurements, at different pump fluences.



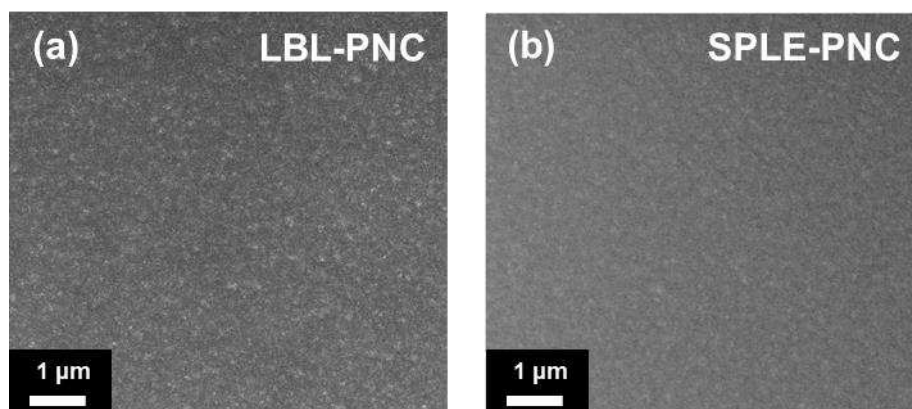
Supplementary Fig. 16. Normalized absorption spectra of the PNC films.



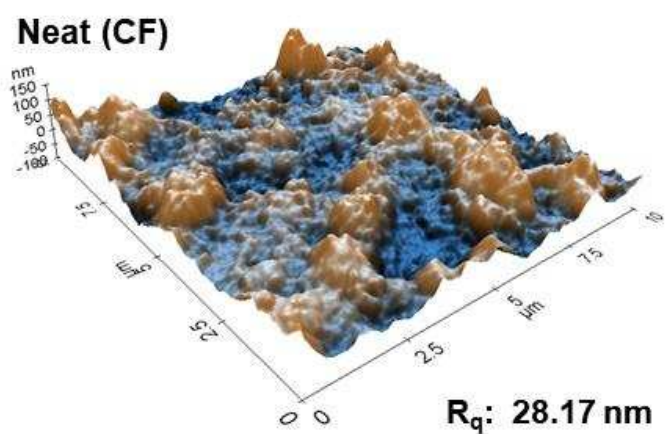
Supplementary Fig. 17. Photo-CELIV current transients of LBL- and SPLE-PNC matrices for (a) hole and (b) electron, collected at various delay times from pump pulse. Estimated carrier mobility and extracted carrier density, including recombination lifetime, of the PNC matrices as a function of delay time for (c) hole and (d) electron, respectively. For mobility plots, the averaged mobility $\langle \mu \rangle$, as a representative mobility of each PNC system, was depicted as a solid line.



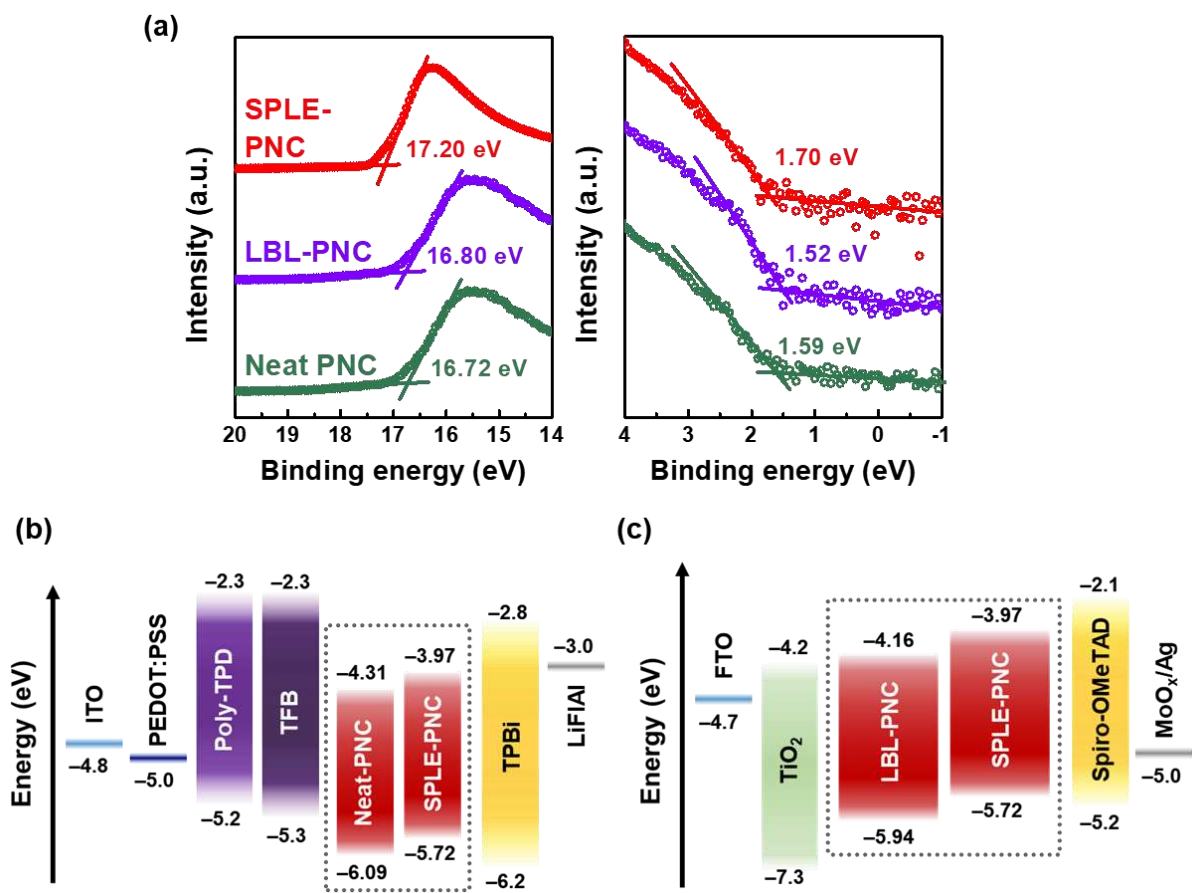
Supplementary Fig. 18. AFM surface profiles of (a) neat (octane dispersion with a concentration of 10 mg mL^{-1}), (b) LBL-, and (c) SPLE-PNC (CF dispersion with a concentration of 150 mg mL^{-1}) films, respectively. For each film, the value of R_q (root-mean-square of height profile), an indicator of surface roughness, is labeled.



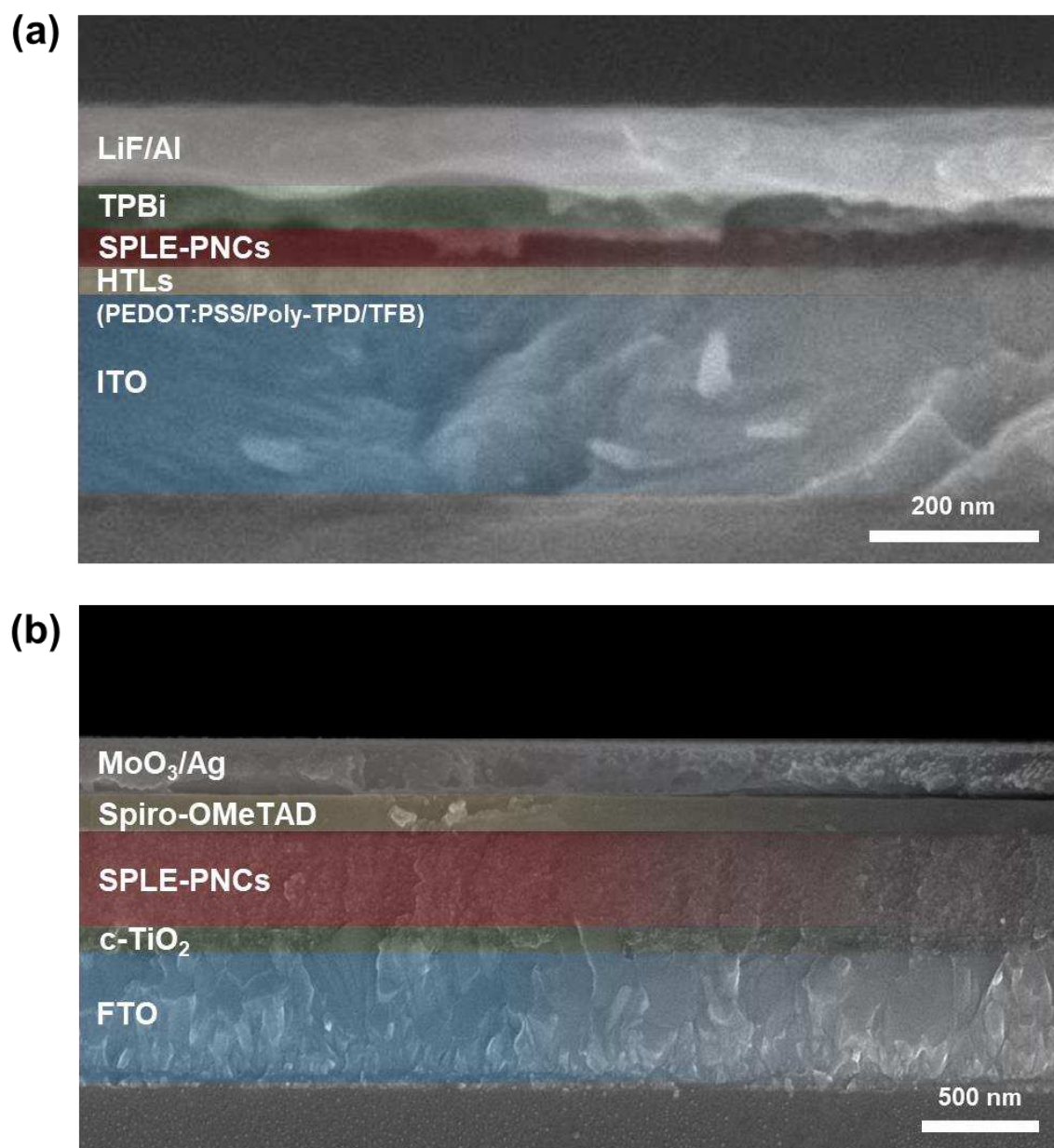
Supplementary Fig. 19. Surface SEM images of (a) LBL- and (b) SPLE-PNCs, respectively.



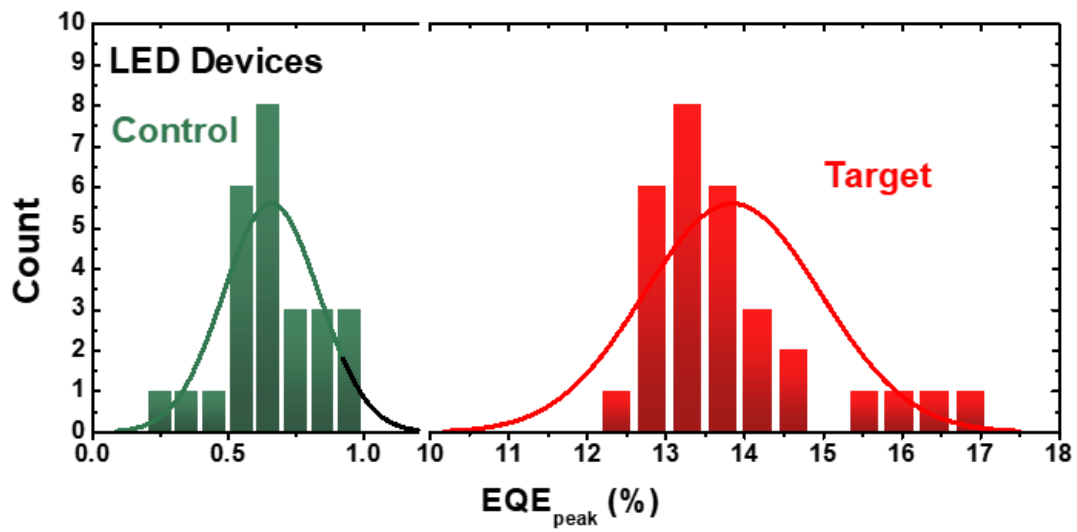
Supplementary Fig. 20. AFM surface profile of neat PNC film prepared with CF at a concentration of 150 mg mL^{-1} . The R_q of the film is also labeled.



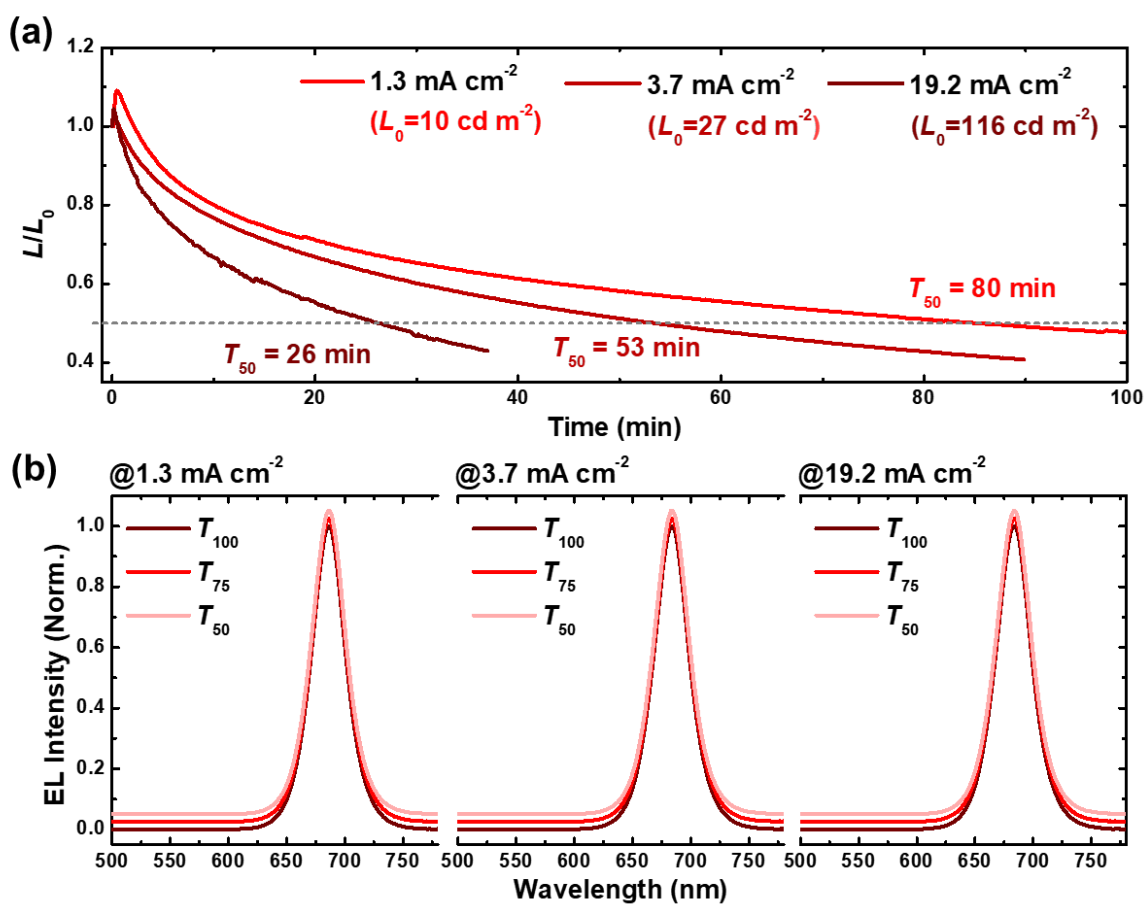
Supplementary Fig. 21. (a) UPS Spectra of the PNC films. Constructed energy level diagrams of (b) LED and (c) PV devices.



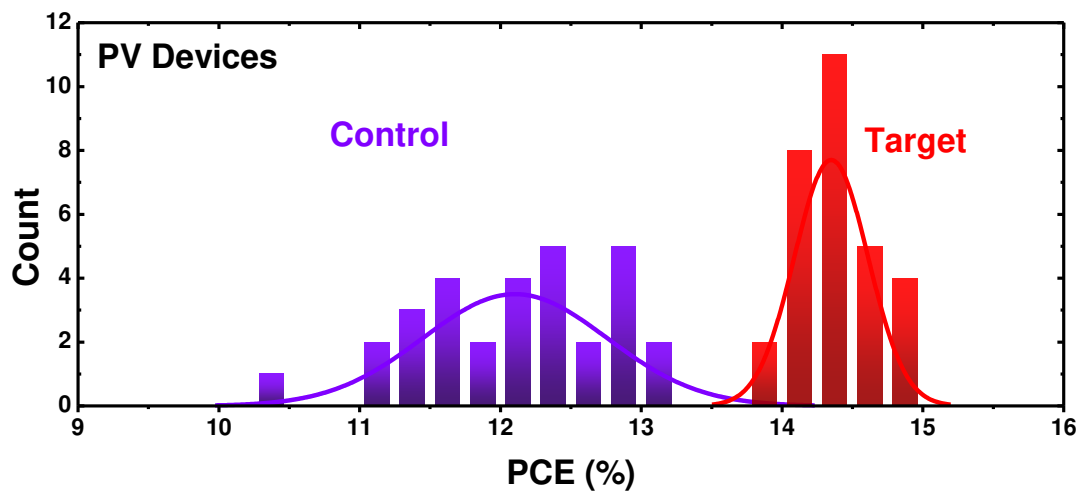
Supplementary Fig. 22. Cross-sectional SEM images of (a) LED and (b) PV devices.



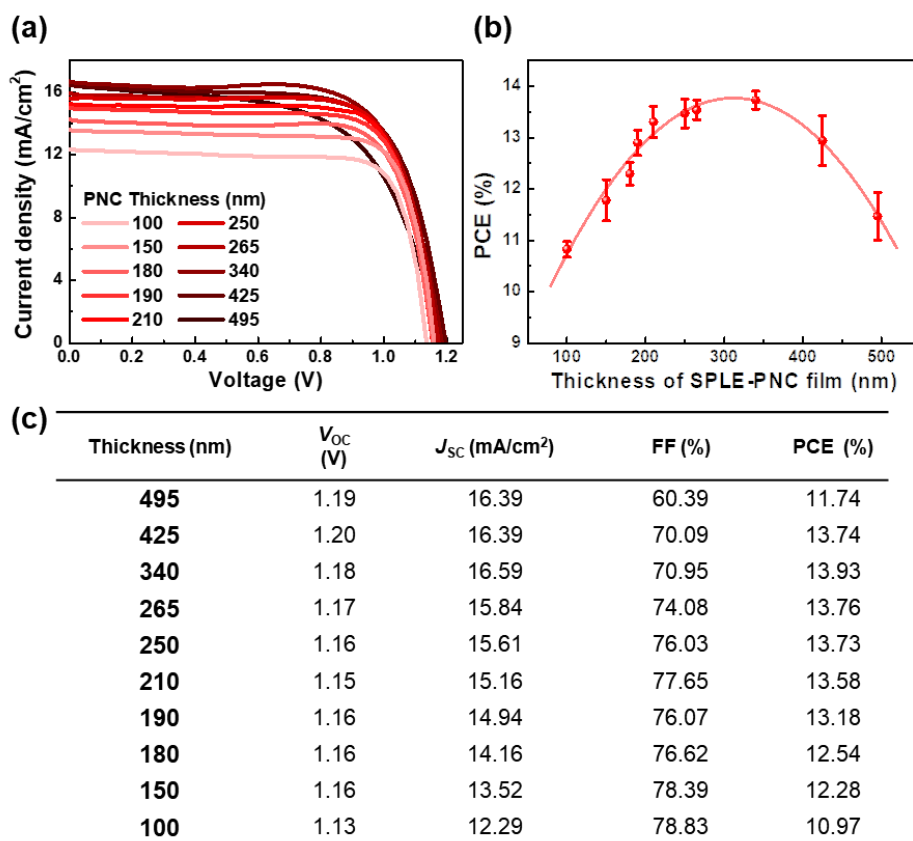
Supplementary Fig. 23. Histograms of EQE_{peak} demonstrated by control and target LED devices, based on the performances of 30 individual devices



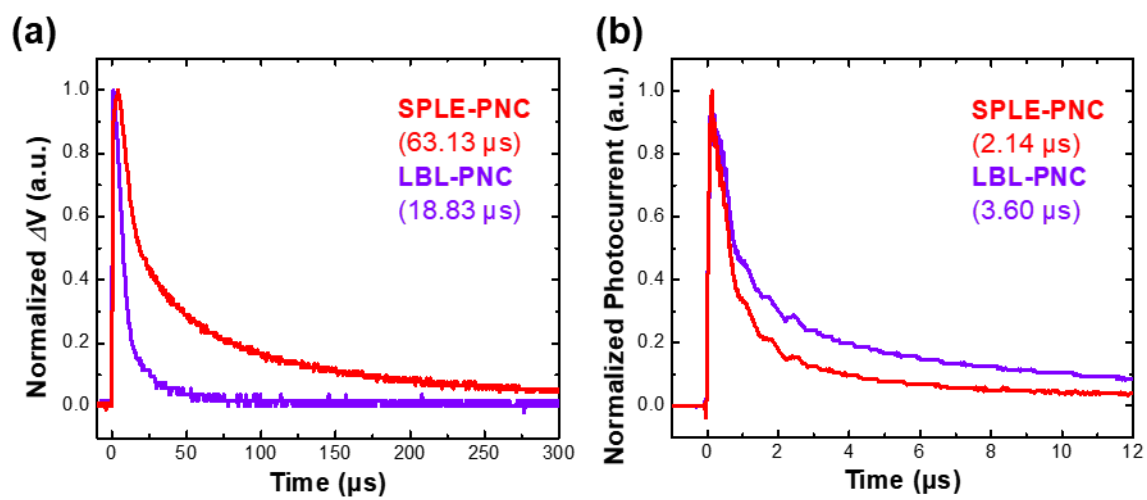
Supplementary Fig. 24. (a) Operation stability of target LED at different levels of current injection and (b) corresponding EL spectra of target LED at different timepoints.



Supplementary Fig. 25. Histograms of PCE demonstrated by control and target PV devices, based on the performances of 30 individual devices



Supplementary Fig. 26. (a) Representative J - V curves and (b) PCE statistics of target PVs with different thickness of SPLE-PNC film. (c) A summary of photovoltaic performances of the PVs as a function of SPLE-PNC film thickness.

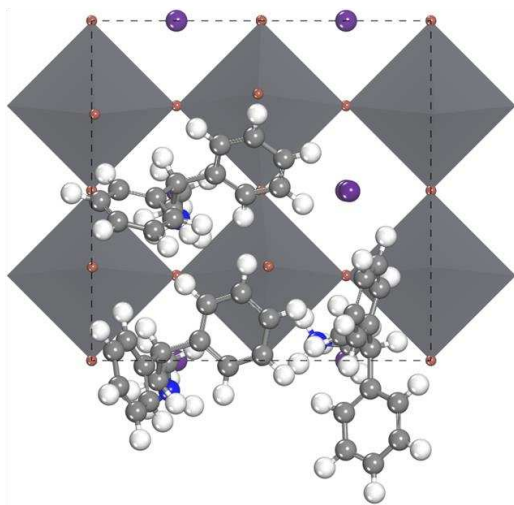


Supplementary Fig. 27. (a) Transient photovoltage and (b) photocurrent of the PVs.

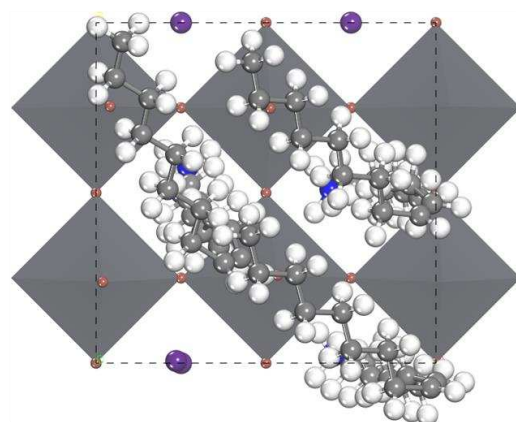
Supplementary Note 3. MD simulation details

We systemically performed molecular dynamics (MD) simulations using the FORCITE module in the Materials Studio with universal force field for reasonable dynamics results. The slab models of MD simulation were designed to observe the motions of the ligand (@CsPbI₃) and compare the dynamics of water penetration through the ligand on the surface depending on the ligand types (**Fig. 4. d-g**). Here, we used 75% ligand coverage on the CsPbI₃ surface, which was confirmed by exploring coverage-dependent ligand binding energy calculations as shown in **Supplementary Fig. 28**. And we adjusted the number of water molecules to the density of water in a given volume. The MD simulations were performed in a canonical ensemble (*NVT*) with a Nose-Hoover thermostat^[6,7] using the fully relaxed geometry at 298 K during 500 ps simulation time with a 2 fs time step. Then, we analyzed water concentration during MD simulation to compare the degree of water penetration according to ligands.

(a) **DPAm⁺@CsPbI₃**
Coverage 75%



(b) **OAm⁺@CsPbI₃**
Coverage 75%



Supplementary Fig. 28. Top view of the DPAm⁺- and OAm⁺- bound CsPbI₃ surface structures at a maximum ligand coverage (75%) used for the MD simulations as multi-ligand surface structure.

Supplementary Table 1. Summarized LED performances based on CsPbI₃ PNCs reported to date.

Treatment	Perovskite	Emission peak [nm]	EQE [%]	Operation Stability [T ₅₀]	L _{max} [cd/m ²]	Reference
Metal Ion Doping	Zn-alloyed PNC	682	15.1	-	2202	[8]
	Sr-doped PNC	678	5.92	2 h	1250	[9]
	Zr-doped PNC	686	13.7	-	14725	[10]
	Zn-doped PNC	684	10.3	-	1605	[11]
	Ni-doped PNC	~690	7.0	0.54 h	830	[12]
	Sr-doped PNC	687	17.1	0.6 h	586	[13]
Surface Ligand Engineering	¹ L-PHE-PNC	675	10.21	-	407	[14]
	² OPA- PNC	682	12.6	0.8 h	10171	[15]
	³ SDS- PNC	~690	8.4	-	830	[16]
	⁴ PMA- PNC	690	17.8	317h (in N ₂)	618	[17]
	⁵ SPLE-PNC (DPAI)	684	17.00	~1.3 h	657	Our work

¹L-PHE: L-phenylalanine

²OPA: Octylphosphonic acid

³SDS: Sodium dodecyl sulfate

⁴PMA: poly(maleic anhydride-*alt*-1-octadecene)

⁵DPAI: 3,3-Diphenylpropylammouium iodide

Supplementary Table 2. Summarized PV performances based on CsPbI₃ PNCs reported to date.

Fabrication process	Perovskite	PCE [%]	Condition	Stability	Reference
	¹ NaOAc treated PNC	12.4	RH 20%, 25°C	90% retention for 22 days	[18]
	² CsAc post-treatment	14.1	RH 40%, 25°C	70% retention for 54 hours	[19]
	Zn-doped PNC	14.8	RH 20~30%, 25°C	62% retention for 350 hours	[20]
LBL	³ PEAI post-treatment	14.1	RH 20~25%, 25°C	90% retention for 15 days	[21]
	⁴ DPA treated PNC	14.9	RH 30~40%, 20- 30°C	70% retention for 130 hours	[22]
	Glycine treated PNC	13.66	RH 20%, 20- 30°C	87% retention for 10 days	[23]
	⁵ 4-MP post-treatment	14.25	RH 20~25%, 20- 30°C	60% retention for 30 day	[24]
	⁶ TBI- ⁷ TOP treated PNC	16.2	RH ~10%, 25°C	83% retention for 10 days	[25]
Ink	SPLE-PNC (DPAI)	14.92	RH 20~30%, 25°C	73% retention for 101 days	Our work

¹NaOAc: Sodium acetate

²CsAc: Cesium acetate

³PEAI: Phenethylammonium iodide

⁴DPA: n-Dipropylamine

⁵4-MP: *p*-Mercaptopyridine

⁶TBI: *tert*-Butyl iodide

⁷TOP: Trioctylphosphine

References

- [1] Delley, B. An all-electron numerical method for solving the local density functional for polyatomic molecules. *J. Chem. Phys.* **92**, 508–517 (1990).
- [2] Delley, B. From molecules to solids with the DMol³ approach *J. Chem. Phys.* **113**, 7756–7764 (2000).
- [3] Klamt, A & Schuurmann, G. COSMO: a new approach to dielectric screening in solvents with explicit expressions for the screening energy and its gradient. *J. Chem. Soc., Perkin Trans. 2* 799-805 (1993).
- [4] Delley, B. The conductor-like screening model for polymers and surfaces. *Mol. Simul.*, **32**, 117-123 (2006).
- [5] Chiba, T. et al. Anion-exchange red perovskite quantum dots with ammonium iodine salts for highly efficient light-emitting devices. *Nat. Photon.* **12**, 681–687 (2018).
- [6] Shuichi, N. Constant temperature molecular dynamics methods. *Prog. Theor. Phys. Suppl.* **103**, 1 (1991).
- [7] Hoover, W. G. Canonical dynamics: equilibrium phase-space distribution. *Phys. Rev. A* **31**, 1695–1697 (1985).
- [8] Shen, X. et al. Zn-alloyed CsPbI₃ nanocrystals for highly efficient perovskite light-emitting devices. *Nano Lett.* **19**, 1552–1559 (2019).
- [9] Yao, J.-S. et al. Few-nanometer-sized α -CsPbI₃ quantum dots enabled by strontium substitution and iodide passivation for efficient red-light emitting diodes. *J. Am. Chem. Soc.* **141**, 2069–2079 (2019).
- [10] Lu, M. et al. Bright CsPbI₃ perovskite quantum dot light-emitting diodes with top-emitting structure and a low efficiency roll-off realized by applying zirconium acetylacetonate surface modification. *Nano Lett.* **20**, 2829–2836 (2020).
- [11] Zhang, X. et al. Energy level modification with carbon dot interlayers enables efficient perovskite solar cells and quantum dot based light-emitting diodes. *Adv. Funct. Mater.* **30**, 1910530 (2020).
- [12] Liu, M. et al. Ni²⁺-doped CsPbI₃ perovskite nanocrystals with near-unity photoluminescence quantum yield and superior structure stability for red light-emitting devices. *Chem. Eng. J.* **413**, 127547 (2021).
- [13] Chen, C. et al. Highly stable CsPbI₃:Sr²⁺ nanocrystals with near-unity quantum yield enabling perovskite light-emitting diodes with an external quantum efficiency of 17.1%. *Nano Energy* **85**, 106033 (2021).
- [14] Shi, J. et al. In situ ligand bonding management of CsPbI₃ perovskite quantum dots enables high-performance photovoltaics and red light-emitting diodes. *Angew. Chem. Int. Ed.* **59**, 22230–22237 (2020).

- [15] Liu, M. et al. Surface ligand engineering-assisted CsPbI₃ quantum dots enable bright and efficient red light-emitting diodes with a top-emitting structure. *Chem. Eng. J.* **404**, 126563 (2021).
- [16] Zhang, J. et al. Highly luminescent and stable CsPbI₃ perovskite nanocrystals with sodium dodecyl sulfate ligand passivation for red-light-emitting diodes. *J. Phys. Chem. Lett.* **12**, 2437–2443 (2021).
- [17] Li, H. et al. Efficient and stable red perovskite light-emitting diodes with operational stability >300 h. *Adv. Mater.* **33**, 2008820 (2021).
- [18] Kim, J. et al. Alkali acetate-assisted enhanced electronic coupling in CsPbI₃ perovskite quantum dot solids for improved photovoltaics. *Nano Energy* **66**, 104130 (2019).
- [19] Ling, X. et al. 14.1% CsPbI₃ perovskite quantum dot solar cells via cesium cation passivation. *Adv. Energy Mater.* **9**, 1900721 (2019).
- [20] Bi, C. et al. Stable CsPb_{1-x}Zn_xI₃ colloidal quantum dots with ultralow density of trap states for high-performance solar cells. *Chem. Mater.* **32**, 6105–6113 (2020).
- [21] Kim, J. et al. Hydrophobic stabilizer-anchored fully inorganic perovskite quantum dots enhance moisture resistance and photovoltaic performance. *Nano Energy* **75**, 104985 (2020).
- [22] Wang, Y. et al. Surface ligand management aided by a secondary amine enables increased synthesis yield of CsPbI₃ perovskite quantum dots and high photovoltaic performance. *Adv. Mater.* **32**, 2000449 (2020).
- [23] Jia, D. et al. Dual passivation of CsPbI₃ perovskite nanocrystals with amino acid ligands for efficient quantum dot solar cells. *Small* **16**, 2001772 (2020).
- [24] Khan, J. et al. Tuning the surface-passivating ligand anchoring position enables phase robustness in CsPbI₃ perovskite quantum dot solar cells. *ACS Energy Lett.* **5**, 3322–3329 (2020).
- [25] Jia, D. et al. Surface matrix curing of inorganic CsPbI₃ perovskite quantum dots for solar cells with efficiency over 16%. *Energy Environ. Sci.* **14**, 4599–4609 (2021).